HOKKAIDO UNIVERSITY

Title	Understanding intraseasonal propagating oscillation in air temperature and its association with heatwaves over Eurasia during boreal summer
Author(s)	宮, 湛秋
Degree Grantor	北海道大学
Degree Name	博士(理学)
Dissertation Number	甲第16528号
Issue Date	2025-06-30
DOI	https://doi.org/10.14943/doctoral.k16528
Doc URL	https://hdl.handle.net/2115/95732
Type	doctoral thesis
File Information	Zhanqiu_Gong.pdf

Hokkaido University Collection of Scholarly and Academic Papers : HUSCAP

Thesis for a Doctorate

博士学位論文

Understanding intraseasonal propagating oscillation in air temperature and its association with heatwaves over Eurasia during boreal summer

（北半球夏季におけるユーラシア季節内気温振動の伝播と熱波との関連性）

氏名

宮　湛秋

Zhanqiu Gong

北海道大学大学院理学院

自然史科学専攻

2025 年 06 月

Abstract

The intraseasonal propagating oscillation in air temperature over Eurasia during boreal summer can cause extreme meteorological events such as heatwaves (HWs), which pose widespread and substantial risks on human livelihoods. Previous studies mainly focused on the quasi-stationary nature of the Eurasian intraseasonal oscillations and their effects on the HWs. However, the understanding of their propagating properties and connection with summer HWs over Eurasia still remains elusive. Therefore, in this study, we aim to investigate the characteristics and mechanisms of the propagating oscillations in air temperature in the lower troposphere over Eurasia during boreal summer and establish its linkage with HWs. First, we examine eastward propagation signals using complex empirical orthogonal function (CEOF) method. The summer air temperature anomalies over Eurasia propagates eastward. The upper-tropospheric geopotential height and meridional wind anomalies are closely associated with the lower-level air temperature anomaly and both anomalies propagate eastward. This indicates that the low-level temperature eastward propagation may be attributed to the upper-tropospheric forcing. According to the temperature budget analysis, it is found that the horizontal temperature advection plays a critical role in driving this eastward propagation, while the diabatic heating rate provides partial compensation. Further decomposition results show that the meridional temperature advection playing a key role in the eastward propagation. The vertical components in the adiabatic process also play a significant role contributing to temperature eastward propagating oscillation. Subsequently, by employing a metric designed to quantify the intensity of propagation signals, a total of nine years which exhibits the strongest propagating signals are identified. A close association between the eastward propagating HWs and reconstructed air temperature anomalies of CEOF mode 1 can be observed in the years with strong values of the amplitude metric, which

indicates a robust linkage. Our results can reinforce the understanding of summer intraseasonal oscillations over Eurasia, and it may also contribute to future monitoring and forecasting capabilities.

Table of Contents

1. Introduction **5**

2. Data and Methods **9**

2.1 Data **9**

2.2 Methods **9**

2.2.1 Data processing **9**

2.2.2 Complex EOF **10**

2.2.3 Atmospheric temperature budget equation **11**

2.2.4 Heatwave definition **13**

2.2.5 Statistical analysis **14**

3. Results **15**

3.1 Propagating oscillations in summer air temperature over Eurasia **15**

3.2 Thermodynamic features based on temperature budget analysis **18**

3.3 Amplitude metric for measuring the intensity of propagating signals **22**

3.4 The association between propagating oscillations and HWs **22**

4. Conclusions and discussion **26**

4.1 Conclusions **26**

4.2 Discussion **27**

Data Availability Statement **30**

Acknowledgments **31**

References **32**

Figures **39**

1. Introduction

The atmospheric intraseasonal oscillations (ISOs) are generally defined as large-scale atmospheric fluctuations with periods ranging from 10 to 90 days. The ISOs are acknowledged to be important atmospheric phenomena and have been extensively studied over the tropical region featured with a 30-60-day eastward propagation, known as the Madden-Julian oscillation (Madden and Julian, 1972).

The ISO also exists in the mid-high latitudes, especially over the Eurasian continent (Ding and Wang, 2007; Kikuchi and Wang, 2009). Since their recognition in the 1950s, Eurasian ISOs have been extensively studied, particularly in winter, when the dominant mode exhibits eastward propagation with a 10-30-day timescale (Namias, 1950; Rex, 1950; Yao et al., 2016; Xiu et al., 2022). Recently, the summer Eurasian ISOs have attracted increasing attentions, which can serve as an effective source for subseasonal predictions of climate variability, benefiting areas vulnerable to the climate change (Vitart and Robertson, 2018; Qi and Yang, 2019).

The summer Eurasian ISOs exhibit diverse characteristics in terms of propagation and periodicity over the mid-high latitudes of the Eurasian continent, where the ISOs feature zonally wave-train structures are trapped along the polar front jet (Iwao and Takahashi, 2008; Huang et al., 2014). The summer ISOs along the polar front jet, which emanate eastward from near Scandinavia and extend across the Ural Mountains and farther toward East Asia, are distinct from the ISOs along the subtropical westerly jet that propagate from the north Atlantic and pass through central Asia to Southeast Asia (Fujinami and Yasunari, 2004; Ding and Wang, 2007). Along the polar front jet, a dominant Eurasian summer ISO mode exhibits eastward propagation with a 10-30-day timescale (Fukutomi et al., 2012; Zhu and Yang, 2021). Besides, a westward-propagating ISO mode is also recognized along the polar front jet varies at a period of 10-50 days (Yang et al., 2013,

2022; Zhao et al., 2017). In addition to the propagating ISOs, observations also revealed ISOs that show geographically stationary characteristics, which are referred to as standing ISOs (Watanabe et al., 2004; Xu et al., 2020). Here we focus on the eastward-propagating ISO along the polar front jet with a 10-30-day timescale as it is a major contributor to the total 10-90-day intraseasonal variability, contributing to downstream atmospheric fluctuations and providing a precursor signal for the potential predictability of extreme weather events (Vitart and Robertson, 2018; Wang et al., 2023).

The summer propagating Eurasian ISOs along the polar front jet play an essential role in regulating the intraseasonal climate variability over Eurasia. Previous studies have been shown their influence on precipitation, sea ice, and blockings over the mid-high latitudes of Eurasia (Fukutomi et al., 2012; Yang et al., 2013; Fan and Yang, 2023; Zhu et al., 2023). Over the northern Eurasia, extending from the east of Lake Baikal to the Far East Asian coast along 50-60°N, the summer precipitation variability is influenced by eastward-propagating ISOs trapped in the polar front jet with periods of 9, 15, and 45 days (Fukutomi et al., 2012). Additionally, the ISOs along the subtropical westerly jet, which influence lower-latitude climate variability including monsoon over South Asia and rainfall variability over East Asia (Ding and Wang, 2007; Jiang and Lau, 2008; Li and Mao, 2019; Liu et al., 2020), coexist with the ISOs along the polar front jet and jointly contribute to the precipitation intraseasonal variability over North Asia and Siberia (Iwao and Takahashi, 2008). Compared to the precipitation, the intraseasonal variability of summer air temperature has received less attention. Several studies focus on the impacts of the eastward-propagating ISO along the polar front jet with a period of 10-30 days on the summer air temperature intraseasonal variability in northeast China (Liang et al., 2018; Wang et al., 2023), while the air temperature variability in the mid-to-high latitudes of the Eurasian continent remains

less explored. Moreover, the underlying mechanisms of ISO-related climate variability are not yet fully understood.

The role of propagating Eurasian summer ISOs along the polar front jet in extreme weather events, such as heatwaves (HWs), has rarely been explored based on individual events, while previous studies have primarily focused on the influence of standing ISOs on HWs. For instance, the Eurasian summer standing ISOs, which exhibit geographically stationary characteristics, have impacts on regional persistent HWs including their occurrences, formation, and maintenance (Teng et al., 2013; Kornhuber et al. 2019; White et al., 2022). On the other hand, Minobe et al. (2022) found that, in 2021, a quasi-biweekly propagating oscillation over Eurasia is related to an unprecedented eastward propagating HW around northern Japan and Eurasia from mid-July to early August. This propagation oscillation is found to exhibit similar periods, propagation speeds, and regions to the 15-day Eurasian summer ISO mode reported by Fukutomi et al. (2012), which focus on the intraseasonal precipitation variability.

The connection between propagation signals of Eurasian summer ISO and propagating HWs was explored based on individual events. However, whether this connection remains robust across different years has yet to be investigated. Moreover, the dominant ISO mode that captures the most significant pattern in summer air temperature variability over the entire Eurasia still requires comprehensive investigation. Furthermore, the relative contributions of atmospheric circulation and thermodynamic processes to the propagation of intraseasonal air temperature variability are not fully addressed. To address these gaps, this study aims to identify the dominant propagating mode of summer air temperature intraseasonal variability over Eurasia and examine the possible mechanisms governing its propagation. Therefore, a Complex Empirical Orthogonal Function (CEOF; Dommenget and Latif, 2002; O'Kane et al., 2014) analysis is performed. This method

allows for efficient detection of propagating features on the boreal summer air temperature intraseasonal variability. The mechanisms underlying this propagation are then examined through a heat budget analysis. Additionally, the potential linkage to the propagating HWs is also investigated.

The remaining sections are structured as below. In Section 2, data and methods are presented. Our main results are shown in Section 3. Specifically, the features of intraseasonal propagating signals of air temperature are investigated in Section 3.1, and its mechanisms are explored in Section 3.2. In Section 3.3, we establish a metric to measure the propagation intensity. Section 3.4 demonstrate the connection between intraseasonal propagating oscillations and HWs. Finally, the conclusions and discussion are provided in Section 4.

2. Data and Methods

2.1 Data

We utilize 6-hourly atmospheric dataset of the Japanese 55-year Reanalysis product (JRA-55; Kobayashi et al., 2015; Harada et al., 2016), including the air temperature, zonal and meridional wind, geopotential height, large-scale condensation heating rate, convective heating rate, vertical diffusion heating rate, solar radiative heating rate, and longwave radiative heating rate covering the period from 1979 to 2021. These variables mentioned above are provided with a horizontal resolution of $1.25° \times 1.25°$. The JRA-55 dataset was chosen for its good representation of atmospheric ISO in mid-high latitudes (Kikuchi, 2020). To examine the robustness of the analyses, we also examined the Fifth Generation ECMWF Reanalysis dataset (ERA5; Hersbach et al., 2020) with a horizontal resolution of $0.25° \times 0.25°$ for the same period as the JRA-55 data.

To investigate the characteristics of HWs, daily maximum surface air temperature obtained from the Climate Prediction Center (CPC) for the same period with a $0.5° \times 0.5°$ spatial resolution is employed. The gridded temperature data from CPC have key advantages, such as considering the orographic effects, displaying less bias in representing extreme values compared to other gridded data products (Behnke et al., 2016), and having consistent quantity and improved quality (Sun et al., 2018).

2.2 Methods

2.2.1 Data processing

In JRA-55, we first obtained daily mean fields by averaging the 6-hourly data at 00, 06, 12, and 18 UTC. Then, for all the daily temperature datasets, we remove the linear trend grid-by-grid to exclude disturbances of global warming. After that, we calculated the anomalies at each grid

point by subtracting the climatology, which was determined as the sum of the long-term mean and the first three harmonics of the seasonal cycle using harmonic analysis (Kirkyla and Hameed, 1989).

2.2.2 Complex EOF

Complex Empirical Orthogonal Function (CEOF) is widely used for analyzing propagating waves (Rasmusson et al., 1981; Barnett, 1983; Horel, 1984; Navarra and Simoncini, 2010). This method extends the conventional EOF to the complex domain using Hilbert transform (Brillinger, 1981). In contrast to the conventional EOF analysis, which can only be used for detecting standing waves, the CEOF method is capable of revealing both phase changes and spatial propagation features (Rasmusson et al., 1981; Enfield and Mestas-Nuñez, 1999; Hannachi et al., 2007).

In this study, the Hilbert transform is conducted first for the daily anomalous air temperature data metric $\boldsymbol{x}(t,s)$ ($t = 1, \dots n$, t denotes time and $s = 1, \dots p$, s is the spatial position) between May 1st and September 30th from 1979 to 2021 as we focus on the air temperature variability during boreal summer. The transformation into a complex data matrix $\boldsymbol{X}(t,s)$ can be written as:

$$\boldsymbol{X}(t,s) = \boldsymbol{x}(t,s) + i\widehat{\boldsymbol{x}}(t,s), \quad (1)$$

where i is imaginary unit, the real part represents the original data array, while the imaginary part ($\widehat{\boldsymbol{x}}(t,s)$) is the Hilbert transform of $\boldsymbol{x}(t,s)$. In this transform, the phase of each component is shifted by $\pi/2$ and the amplitude remains unchanged (Horel, 1984). Then, the output data are trimmed to June-August (JJA) in order to eliminate the edge effects in the time domain.

Similar to conventional EOF analysis, CEOF also solves the eigenfunctions of the covariance matrix:

$$\boldsymbol{C} = \frac{1}{n}\sum_{t=1}^{n} \boldsymbol{X}(t,s)\, \boldsymbol{X}(t,s)^{*\mathrm{T}}, \quad (2)$$

where $*$ is the complex conjugate operator and T denotes the transpose operator. The data is weighted prior to decomposition by the square root of the cosine of latitudes to ensure equal area weighting. The cosine factor was multiplied back in prior to plotting the spatial patterns. The complex eigenvectors and associated complex principal components obtained from $\boldsymbol{C}$ are referred to as CEOFs (CEOF_j) and CPCs (CPC_j) respectively, where j denotes the mode number. The CPCs are normalized to unit variance. Then the spatial patterns of the CEOFs are presented by regressing the anomalous temperature data onto the normalized CPCs.

To better understand a propagating wave pattern, the spatial and temporal amplitudes and phases obtained by the real and imaginary parts of the CEOFs and CPCs are necessary components. The spatial amplitude is estimated as the square root of the squares of real and imaginary CEOFs, and the temporal amplitude is similarly calculated as the square root of the CPC components. The spatial ($\Phi_j(s)$) and temporal ($\theta_j(t)$) phases are estimated as:

$$\Phi_j(s) = \arctan\left[\frac{\mathrm{Im}(\mathrm{CEOF}_j)}{\mathrm{Re}(\mathrm{CEOF}_j)}\right], \quad (3)$$

$$\theta_j(t) = \arctan\left[\frac{\mathrm{Im}(\mathrm{CPC}_j)}{\mathrm{Re}(\mathrm{CPC}_j)}\right], \quad (4)$$

where Re() and Im() represent respectively the real and imaginary parts. From the definition, we can see that the temporal and spatial phases range between $-\pi$ and π. Therefore, in order to avoid inconvenient jumps of 2π and have smooth spatial or temporal variations, the phase unwrapping process is applied (Terradas et al., 2004). This can be achieved by detecting the existence of a wrap where the difference between successive phase values exceeds π and then adjusting these differences by adding or subtracting an appropriate multiple of 2π.

2.2.3 Atmospheric temperature budget equation

The atmospheric air temperature budget equation can be expressed as:

$$\frac{\partial T}{\partial t} = -\boldsymbol{V} \cdot \nabla T + \omega\left(\frac{RT}{pC_p} - \frac{\partial T}{\partial p}\right) + Q_{dia}, \quad (5)$$

where $\frac{\partial T}{\partial t}$ represents the temperature changing rate (TCR) in unit K day^{-1}. Here we estimate the change in air temperature at 850 hPa over time by applying a central difference approximation ($\frac{\partial T}{\partial t} \approx \frac{T(t+\Delta t)-T(t-\Delta t)}{2\Delta t}$, where $\Delta t = 1$ day). $\boldsymbol{V}$ is the horizontal wind vector, p denotes the pressure, C_p ($= 1004.68$ J/kg/K) is the specific heat at constant pressure, R ($= 287$ J/kg/K) is the gas constant of dry air, and ω is the vertical velocity. $-\boldsymbol{V} \cdot \nabla T$ is the horizontal temperature advection (HTADV) and $\omega\left(\frac{RT}{pC_p} - \frac{\partial T}{\partial p}\right)$ represents the vertical components (vertical thermal advection and compression heating; VADHR) in adiabatic heating process. The components we calculated are using daily averaged variables.

Q_{dia} is the diabatic heating rate (DHR) at 850 hPa which is obtained by adding the vertical diffusion heating rate (VDFHR), convective heating rate (CNVHR), large-scale condensation heating rate (LRGHR), longwave radiative heating rate (LWHR), and solar radiative heating rate (SWHR) directly provided by JRA-55 dataset as follows:

$$Q_{dia} = \text{VDFHR} + \text{LWHR} + \text{SWHR} + \text{CNVHR} + \text{LRGHR}, \quad (6)$$

where the VDFHR is related to sensible heating represents the energy transfer without phase change. The latent heating rate (LHR) includes the CNVHR and LRGHR. It is directly related to the total amount of condensation of water vapor and is closely related to the precipitation.

The temporal amplitude based on the first mode of complex principal component (CPC-1) of summer air temperature reflects the intensity of the eastward propagation oscillation across the Eurasian continent over time. Therefore, the metric that represents the variability of the propagating signals during summer can be obtained as the time-averaged absolute amplitude of CPC-1 for each year as given by:

$$P(yr) = \frac{1}{J}\sum_{j=j1}^{j=j2}\left|\tilde{T}_1(yr,j)\right|, (7)$$

where $\tilde{T}_1$ is the temporal amplitude calculated as the square root of real and imaginary CPC-1 of 850 hPa air temperature, *j* is the Julian day with *j1* and *j2* corresponding June 1st and August 31st, and *J* is the number of days during the period (92 days).

2.2.4 Heatwave definition

HWs are defined in many different ways, mainly in the metrics, the thresholds of exceedance, and the duration of a HW event (Robinson, 2001; Fischer and Schär, 2010; Perkins and Alexander, 2013). We selected a minimum number of two consecutive days of daily maximum air temperature to define a heatwave event following prior studies (Anderson and Bell, 2011; Meehl and Tebaldi 2004). The manner in which thresholds of exceedance definition can either be a fixed absolute threshold (physiologically based) or a relative threshold (temperature percentile depends on the local climate; Robinson, 2001). This study adopted a relative threshold (Alexander et al., 2006; Perkins et al., 2012) instead of an absolute threshold to preserve the physical extremes of locations having completely different climatological settings.

Here we define a HW event for each grid point as a spell of at least three consecutive days with daily maximum 2-m air temperature exceeding the 95th percentile threshold. To avoid the influence from high-frequency signals, and also to increase the sampling size, we set a 21-day window to define a threshold (Stefanon et al., 2012; Wang et al., 2017) for each calendar day in JJA (for 43 years from 1979 to 2021, the 21-day window gives a sample size of 903 days).

The time-area integration of HW occurrences between 40°-70°N, 0°-130°E and here we call this indicator as HW area-day. The HW area-day (*I*) is defined as:

$$I(yr) = \sum_t \sum_A D(yr,t,lat,lon)A\,(lat,lon), (8)$$

where $D(yr, t, lat, lon)$ is the heatwave occurrence (1 if a HW event occurs, 0 otherwise), t represents 92 days in JJA. A ($= R^2 \cos(lat) \cdot \Delta lat \cdot \Delta lon$, R is the Earth's radius in km) denotes the grid cell area in the unit km^2.

2.2.5 Statistical analysis

The statistical significance for linear regression analyses is assessed using the two-sided Student's t-test. The effective degrees of freedom are calculated below (Bretherton et al., 1999):

$$N_{eff} = N\left(\frac{1-r_1 r_2}{1+r_1 r_2}\right), \quad (9)$$

where N_{eff} is the effective degrees of freedom, N denotes the data length, r_1 and r_2 represent the lag-1 autocorrelation coefficients.

The phase composite analysis results are compared with the whole boreal summer for significance estimation. The two-sided Student's t-test is applied to judge the statistical significance. The effective degrees of freedom k are estimated by:

$$k = \frac{\left(s_p^2/n_p + s_y^2/n_y\right)^2}{\frac{\left(s_p^2/n_p\right)^2}{n_p - 1} + \frac{\left(s_y^2/n_y\right)^2}{n_y - 1}}, \quad (10)$$

where S_p is the standard deviation of the anomaly field composed for different phases, S_y is the standard deviation of the anomaly field composed for the whole boreal summer, and n represents the sample size (Satterthwaite, 1946; Welch, 1947).

3. Results

3.1 Propagating oscillations in summer air temperature over Eurasia

To investigate the propagation features of intraseasonal oscillations in air temperature at 850 hPa during boreal summer, the CEOF analysis is employed over the Eurasian region (30°-70°N, 0°-130°E). This domain is selected to focus on the mid-to-high latitudes where large-scale intraseasonal oscillations associated with the polar front jet are pronounced. The CEOF mode 1 (CEOF-1) real and imaginary spatial patterns explain 15.7% variability of air temperature (Fig. 1d), and is statistically distinguishable from the rest of the modes, according to the calculation of the error range of eigenvalue proposed by North et al. (1982). The real component of CEOF-1 (Fig. 1a) exhibits a zonal wave-like pattern with alternating positive and negative anomalies from east European plain to the East Asia coastal region. This pattern represents the leading mode of air temperature intraseasonal variations during boreal summer over Eurasia. A similar pattern seen in the imaginary component of CEOF-1 (Fig. 1b), suggesting a zonal wave-like pattern with one wavelength that spans around 3,500 km over Eurasia. With a phase-shifted of $\pi/2$ in the time evolution relative to the real component, the spatial structure of CEOF-1 real component switches signs in the imaginary component, representing paired patterns in quadrature.

The information of spatial amplitudes and phases of the CEOF-1 are used to understand the propagating nature of the presented air temperature zonal wave-like pattern. The spatial amplitudes of CEOF-1 are characterized by a zonal band with large values between 40° and 70°N extends from 30° to 110°E (shadings in Fig. 1c). The region with high amplitude values represents the activity hotspot, where the intensity of intraseasonal air temperature oscillations reaches its peak. The spatial phases of CEOF-1 undergo nearly a complete cycle across the peak amplitude region (contours in Fig. 1c). The variation of the spatial phases with position is a consequence of the

traveling character of the wave. The spatial amplitudes and phases suggest that the intraseasonal oscillation of air temperature exhibits zonal propagation characteristics over Eurasia.

Since the propagating signals of 850 hPa air temperature CEOF-1 are identified, we further calculate its spatial and temporal phases to determine the directions of the propagation signals. It can be observed that the region having large amplitude values occurs between 40° and 70°N while the spatial phase varies linearly with distance from 30° to 110°E (Fig. 1c). Therefore, we calculate the 10-degree latitudinal averaged spatial phases along 40° to 70°N, as shown in Figs. 2a-c. The temporal phase is displayed in Fig. 2d, and the temporal phase varies linearly in time. According to previous studies, the derivative of spatial phases provides a measurement of the local wavenumber k and the time derivative of the temporal phase represents the angular frequency ω (Susanto et al., 1998; Terradas et al., 2004; Hannachi et al., 2007; Majumder et al., 2019). The CEOF-1 of summer air temperature over Eurasia has local wavenumbers around 4 to 5 within 40°-70°N (Figs. 2a-c), respectively. Estimation of the period, computed from a linear least-squares fit to the phases, gives the value of 19.81 as the angular frequency of CEOF-1 (Fig. 2d). The phase speed can be obtained using the relation $c = \omega/k$ from the values of the local wavenumber and angular frequency. The average phase speed along 40° and 70°N is 5.6 m/s. The positive value of phase speed suggests the Eurasian summer air temperature intraseasonal oscillation propagates eastward.

We further examine the variations of surface air temperature to understand the association between surface and lower-level air temperature. Figure 3 shows the spatial patterns of 2-m surface air mean temperature anomalies for JJA from 1979 to 2021 from the JRA-55 dataset. The CEOF results of the 2-m air mean temperature anomalies (Fig. 3) resemble that of the 850 hPa air mean temperature anomalies (Fig. 1). All characteristics of the results in the 2-m air temperature are

consistent with those using 2-m surface air temperature obtained from ERA5 dataset (not shown here), inferring that our results are not affected by the dataset we used. This also indicates that the air temperature intraseasonal propagating oscillations can occur at the surface, further influencing temperature changes and may potentially modulating the local HWs. Here we mainly show the results of 850 hPa air mean temperature anomalies in this study.

To clarify the propagating features of this propagating oscillation, we perform a composite life cycle of 850 hPa air temperature and geopotential height anomalies at 200 hPa based on the real and imaginary CPC-1. In the composite analysis, eight phases are identified using the real and imaginary components of CPC-1 to clearly characterize the evolution of the eastward-propagating oscillation. The angle between the real and imaginary components of CPC-1 varies from 0° to 360° over a complete cycle. Then, the phase space can be divided into eight phases by an angle interval of 45°. Also, the values of amplitude (the square root of the squares of real and imaginary CPC-1) larger than one standard deviation are selected for phase composite. The phase composite of air temperature anomaly at 850 hPa (shadings) and geopotential height anomaly at 200 hPa (contours) during eight phases is displayed in Fig. 4. After phase division, each phase has its circulation characteristics, and different phases can refer to distinctive locations of positive and negative temperature (geopotential height) anomaly centers over mid-high-latitude Eurasia. We show that the whole cycle of the temperature fields using CEOF-1 exhibits eastward propagation, consistent with the upper-tropospheric geopotential height propagation. In Fig. 4, phase 7 and phase 1 represent the real and imaginary CEOF-1 respectively, indicating that the wave patterns of real and imaginary CEOF-1 may be two different phases of the same wave train. In phase 1, the positive air temperature anomalies, accompanied by positive upper-level geopotential height anomalies at 200 hPa, occur around 50°N, 30°E. The positive anomalies propagate eastward, reaching

approximately 50°N, 100°E by phase 8. The composite evolution of upper-level geopotential height anomalies was examined to elucidate the large-scale circulation patterns associated with the life cycle of the air temperature intraseasonal oscillations. The circulation anomalies exhibit an eastward propagating wave train.

To find the maximum variability center in summer, the zonal-vertical distribution of the atmospheric variables in the troposphere averaged over 40°-70°N are also investigated. We regressed the air temperature, meridional wind, and geopotential height anomalies from 1000 hPa to 200 hPa averaged over 40°-70°N onto the real and imaginary CPC-1. A statistically significant propagation signal, which can be linearly explained by CPC-1, is discernible in the projections of the real and imaginary parts of CPC-1 onto the entire layer of air temperature anomaly fields in the troposphere, as evidenced by Figs. 5a and 5d. Not only the temperature signals but also the geopotential height anomalies show similar movement related to the hydrostatic relationship, which can be seen from the vertical cross-sections of the geopotential height fields (Figs. 5b and 5e). The results of the upper-level meridional wind anomalies (Figs. 5c and 5f) follow well with that of the geopotential height anomalies through a geostrophic balance relationship. The maximum amplitudes of the meridional wind and geopotential height anomalies are located around 300 hPa. The observational results show that the lower-level intraseasonal temperature propagating signals are closely coupled with upper-tropospheric height anomalies, as well as upper-level wind changes, indicating the low-level temperature eastward propagation may be attributed to the upper-tropospheric forcing.

3.2 Thermodynamic features based on temperature budget analysis

The temperature budget analysis can elucidate the contributions of the atmospheric heating processes including adiabatic and diabatic heating processes (Holton, 2004), which may relate to the intraseasonal air temperature eastward propagating oscillation over the Eurasian continent. To

access the physical mechanism for the intraseasonal air temperature eastward propagating oscillation using atmospheric heat budget, it is necessary to first address whether a reasonable closure of the heat budget is maintained. The latitudinal averaged values for the anomalous temperature changing rate (TCR), horizontal temperature advection (HTADV), vertical components due to adiabatic heating rate (VADHR), and diabatic heating rate (DHR) between 40° and 70°N for real and imaginary CPC-1 are displayed in Fig. 6. The sum of the values of HTADV, VADHR, and DHR is close to that of TCR, indicating the closure of the atmospheric heat budget. Besides, both HTADV and VADHR resemble the variations of TCR, but DHR shows an opposite signal to TCR. The amplitudes of HTADV are higher than that of VADHR. The results indicated in Fig. 6 further provide evidence that the largest contribution comes from the HTADV, while the role of VADHR in contributing to TCR is relatively smaller. While DHR partially compensates for temperature changes.

The spatial patterns for each component associated with the propagating signals are further examined over Eurasia (Fig. 7). Spatial regression patterns of TCR exhibit statistically significant zonal wavelike patterns (Figs. 7a and 7e). These regression patterns, linearly explained by CPC-1, closely correspond to the spatial patterns of air temperature of CEOF-1. The results for the HTADV exhibit similar structures to those of the TCR, as evidenced by Figs. 7b and 7f. The alignment between the TCR and HTADV indicates that the horizontal temperature advection largely contributes to temperature changes associated with the summer air temperature intraseasonal propagating oscillations. In contrast, the regression patterns of the VADHR exhibit a relatively weak propagating signal with a slight eastward shift (Figs. 7c and 7g). This suggests that the VADHR partially contributes to temperature changes. Furthermore, DHR display nearly opposite polarity to TCR (Figs. 7d and 7h), suggesting that DHR acts to counterbalance the temperature

changes. These results observed in Fig. 7 imply that the horizontal temperature advection is the dominant driver of Eurasian summer air temperature eastward propagating oscillation, accompanied by temperature changes. The contribution role of VADHR is smaller, while the DHR provides partial compensation.

The diabatic heating processes are acknowledged to have effects on the occurrences and maintenance of HW events (Shi et al., 2023). Here we find that DHR compensates for the propagating oscillation. We further conducted regression analysis on the components of the DHR to examine their respective contributions to the eastward propagation of summer air temperature oscillations (Fig. 8). Spatial regression patterns of the latent heating rate, which is associated with the total amount of condensation of water vapor, exhibit statistically significant zonal wavelike patterns similar to those of the DHR (Figs. 8a and 8e). The spatial distributions of the regression coefficients for vertical diffusion heating rate (Figs. 8d and 8h) and longwave radiative heating rate (Figs. 8c and 8g) also exhibit opposite responses to the TCR. Their magnitudes are smaller compared to those of the latent heating rate over the area of wave form pattern are seen. This suggests that the latent heating rate is the main contributor to the compensatory role of the DHR in the temperature changes.

Although the horizontal temperature advection is found to be the critical driver for this eastward propagation, a deeper understanding of whether the zonal or meridional component plays a more significant role remains unclear. The HTADV is further decomposed into zonal and meridional terms to understand their respective contributions. Figure 9 presents the regression maps for anomalous zonal and meridional air temperature advection at 850 hPa regressed on the real and imaginary parts of CPC-1. Significant propagating signals can be seen on both zonal and meridional air temperature advection evidenced by Fig. 9. The zonal air temperature advection

(Figs. 9b and 9e) and the meridional air temperature advection anomalies (Figs. 9a and 9c) exhibit nearly opposite signs and similar amplitudes in response to CPC-1. The propagating signals of the meridional air temperature advection anomalies concentrate between 50° and 70°N, displaying a similar pattern HTADV (Figs. 7b and 7f). The signals of the zonal air temperature advection between 40° and 50°N resemble those of the HTADV over the same area. Over the region where the maximum amplitudes of the intraseasonal air temperature eastward propagating oscillation occur, the horizonal temperature advection are mainly attributed to the meridional component. These results indicate that HTADV plays an important role in air temperature propagating oscillation, while the relative contributions of zonal and meridional temperature advection require further examination.

A further examination of the relative contributions from zonal and meridional temperature advections is necessary to refine our understanding of the adiabatic processes driving the eastward propagating oscillation. To quantify these contributions, Fig.10 exhibits the latitudinal averaged values for the anomalous TCR, zonal and meridional temperature advection, and VADHR between 40° and 70°N for real and imaginary CPC-1. The amplitude of meridional temperature advection is slightly larger than the VADHR. Both variations of meridional temperature advection and VADHR are consistent with the TCR variability. On the other hand, the zonal temperature advection show similar amplitude to that of TCR, but not in phase. This indicates that the meridional temperature advection playing a key role in the propagating oscillation of air temperature. The vertical components in the adiabatic process also remain an important factor in air temperature propagating oscillation.

3.3 Amplitude metric for measuring the intensity of propagating signals

We have identified the eastward propagating characteristics of intraseasonal air temperature oscillation during boreal summer over Eurasia. The intensity of this eastward propagation might vary across different years. Therefore, it is useful to first establish a metric that can measure the variations in the intensity of the propagating signals for each summer season.

The yearly averaged absolute amplitude metrics constructed by CPC-1 of air temperature at 850 hPa using two different datasets are displayed in Fig. 11. The values of the amplitude metrics from two datasets almost same. Therefore, in this study we mainly show the amplitude metric using JRA55 dataset. This metric exhibits interannual variability in the intensity of the propagation signals with a range between 0.6 and 1.3. We then take the values that are greater than plus one standard deviation relative to the mean value as strong values of the yearly absolute amplitude metric. A total of nine years (1983, 1987, 1989, 1999, 2006, 2010, 2014, 2015, and 2021) with strong propagating signals are selected as strong events. The values in the nine strong events show magnitudes almost double those in the weak events. However, this does not directly imply that eastward propagation features are necessarily stronger in these years. Further analysis is needed to determine whether eastward propagation signals are more pronounced in years with strong values compared to those with weak values.

3.4 The association between propagating oscillations and HWs

In order to investigate the relationship between the eastward propagating features in air temperature intraseasonal oscillation and HW events over Eurasia, we first show the time series of amplitude metric based on CPC-1 of air temperature at 850 hPa and time-area integration of HW occurrences during a particular summer season over Eurasia (40-70°N, 0-130°E) from 1979 to 2021 (Fig. 12). The values of the amplitude metric (black line in Fig. 12) indicate the intensity of the

propagating signals. The correlation coefficient between the amplitude metric and the HW area-day index is 0.492 (blue line in Fig. 12; $p < 0.001$ and the effective p-value is computed by replacing the sample size N in the t-statistic with the effective sample size N_{eff} which is computed via the lag-1 autocorrelation coefficients), which is statistically significant. The correlation coefficient indicates that approximately 24% of the variance in HW frequency can be explained by the intensity of propagating signals in summer air temperature intraseasonal variability. This indicates that propagating signal of air-temperature is not a dominant controlling factor for the year-to-year HW occurrences, still it plays an important role in HW variability. Consistent with the moderate correlation between the HW area-day index and the temperature propagation metric, the years in which both metrics exhibit exceptionally high values generally do not always coincide. For instance, in 1988, 1998, 2002, and 2007, the HW area-day index exhibits high values, yet the CEOF amplitude metric remains relatively weak. In the year 2003, a severe European HW event with devastating impacts stands out as an anomalous climatic event. However, it appears moderate when considered at the scale of the entire Eurasian continent, and its propagation signal is relatively weak. In addition, both metrics show consistently strong values in 2010 and 2021. The HW area-day index indicates the strongest peak in 2010, consistent with the wide-spread exceptional HWs. The CEOF amplitude metric also exhibits the peak, but as will be discussed, certain portion of this peak is likely to be related to stationary HWs prevailing. The results suggest that the relationship between Eurasian air temperature intraseasonal eastward propagating oscillation and HW events needs further analysis.

We then first examine the spatiotemporal variations of the propagation signals by reconstructing the 850 hPa air temperature anomalies based on the CEOF-1. This reconstruction captures the spatiotemporal characteristics of the air temperature intraseasonal oscillation, emphasizing its dominant eastward propagation pattern. The reconstructed air temperature

anomalies of CEOF-1 at 850 hPa, averaged between 40°-70°N, are shown as contours in Fig. 13. The values displayed in Fig. 13 reflect the intensity of the eastward propagating signals in air temperature intraseasonal oscillation across Eurasia during summer. The propagating signals are confined to the Eurasian continent and lack the spatial characteristics associated with the circumglobal waves. The reconstructed air temperature anomalies exhibit eastward propagation, which are more pronounced in years with strong values of the amplitude metric than that in years with weak values of the amplitude metric (Fig. 14). The results suggest that the amplitude metric is useful for quantifying the variations in the intensity of intraseasonal air temperature eastward propagating oscillation over Eurasia during boreal summer.

The variations of eastward propagation of air temperature may potentially modulate the HWs. Therefore, we further analyze the daily 2-m maximum air temperature anomalies that satisfy the HW definition averaged between 40-70°N (shadings in Fig. 13) and overlay them onto the reconstruction field (contours in Fig. 13). The eastward propagation signals in Eurasian HWs can be observed in Fig. 13, accompanied by the reconstructed air temperature anomalies of CEOF-1, although the connection remains limited to some extent. In the years 1983, 1987, and 1989, HWs are less frequent compared to other years but still exhibit eastward propagation characteristics for mid-August in 1983 (Fig. 13a), early-August in 1987 (Fig. 13b), and early-July in 1989 (Fig. 13c). In 2010, when quasi-stationary HWs were dominant, the HW events occurring in June exhibited an eastward propagation characteristic (Fig. 13f). The eastward propagating signals in HWs can also be found for early-July in 1999 (Fig. 13d) and 2006 (Fig. 13e), early-August in 2014 (Fig. 13g), early-June in 2015 (Fig. 13h), and mid-June in 2021 (Fig. 13i). The frequency of the occurrences of propagating HWs in years with weak values of the amplitude metric is much less than that in years with the strongest values (Fig. 14). These results provide evidences that the

eastward propagation of air temperature intraseasonal oscillation during summer is associated with the propagation characteristics of HWs.

Figure 14 is similar to Fig. 13 but for nine years with the weakest values of the amplitude metric. The occurrences of reconstructed air temperature anomalies exhibiting eastward propagation are much fewer in years with weak values of the amplitude metric than in years with strong values. The frequency of propagating HWs also shows similar results. The eastward propagating HWs can only be found in early-August 2000 (Fig. 14e) and mid-July 2012 (Fig. 14g). In 1985, HWs can hardly be observed (Fig. 14a). For other years, HWs that can be found in August 1997 (Fig. 14d), mid-July 1990 (Fig. 14b), 1993 (Fig. 14c), 2013 (Fig. 14h), and 2018 (Fig. 14i) show no propagating signals. Therefore, we can conclude that the eastward propagating signals are more pronounced in years with strong values of the amplitude metric than that in years with weak values of the amplitude metric.

Furthermore, our results are not sensitive to the definitions of HWs (Fig. 15). In Fig. 15, the HW is defined as at least six consecutive days with 2-m mean air temperature exceeding the 90th percentile threshold. The results are similar to that of Fig. 13, providing evidence that there is a close association between propagating HWs and reconstructed air temperature anomalies over Eurasia in the years with strong intensity propagation signals based on the amplitude metric, indicating a robust linkage between the propagating HWs and the intraseasonal air temperature eastward propagating oscillation.

4. Conclusions and discussion

4.1 Conclusions

The structure and propagation features of intraseasonal air temperature oscillation at 850 hPa over Eurasia during the boreal summer are investigated using JRA55 reanalysis data. Based on CEOF, linear correlation, and composite analysis, we found that the intraseasonal air temperature anomaly over Eurasia exhibits an eastward propagation. The temperature signal propagates eastward at an averaged zonal speed phase of 5.6 m/s, which is around 4.4° longitude per day. Associated with the southeastward propagation of the intraseasonal surface temperature signal, the geopotential height anomaly also propagates eastward. The lower-level air temperature and upper-level geopotential height and meridional wind anomalies are closely coupled, indicating the low-level temperature eastward propagation may be attributed to the upper-tropospheric forcing.

To understand the possible mechanisms of eastward propagating oscillation, we conducted an atmospheric temperature budget analysis at lower-level. By regressing each component onto the CPC-1, it is found that the horizontal temperature advection is crucial in driving this eastward propagating oscillation. Further decomposition of horizontal temperature advection show that the meridional temperature advection playing a key role in the propagating oscillation of air temperature over the region where the maximum amplitudes of propagation signals occur. In addition, our results show that the upper-level geopotential height and meridional wind anomalies reveal eastward propagating wave-like structures, which are coupled with the eastward propagation of lower-level air temperature. The variations of the upper-level geopotential height and meridional wind fields lead to changes in the low-level temperature gradient and hence the meridional temperature advection, resulting in the eastward propagation of the anomalous air temperature. The vertical components in the adiabatic process also remains a significant part

contributing to propagating oscillation. While the diabatic heating rate provides partial compensation role. While not the primary focus of this study, potential vorticity conservation may provide a complementary dynamical perspective, particularly since air temperature is not a conserved quantity at a specific level.

An amplitude metric was established to measure the intensity of propagating signals based on the CPC-1. Further examination on the spatiotemporal variations of the reconstructed the 850 hPa air temperature anomalies of CEOF-1 and HWs was conducted to explore the linkage between air temperature intraseasonal eastward propagating oscillation and HWs during summer over Eurasia. We selected nine years in total with strong intensity of propagating signals, where we also identified the eastward propagating HW events. The amplitude metric is useful for quantifying the variations in the intensity of intraseasonal air temperature eastward propagating oscillation. Additionally, a close relationship between reconstructed air temperature anomalies of CEOF-1 and eastward propagating HWs over Eurasia can be observed, particularly in the years with strong values of the amplitude metric, suggesting a robust linkage.

4.2 Discussion

Several points should be further considered. Firstly, the propagating signal speed obtained from CEOF analysis are likely linked to the Rossby waves. Since Hilbert transform in the CEOF analysis is applied along the time dimension, the resulting propagation characteristics represent the phase speed of the wave pattern. To estimate the theoretical Rossby wave phase speed, we use the climatological summer-mean (JJA) zonal wind at 300 hPa, averaged over the Eurasian continent. This level is typically where Rossby waves are pronounced. The resulting mean background wind speed is approximately 10 m/s during JJA averaged over Eurasia (Orsolini and Sorteberg, 2009; Dong et al., 2022). Assuming an estimated zonal wavelength of 3500-4000 km,

we obtain a theoretical zonal phase speed of approximately 5-6 m/s, which is in close agreement with the propagation speed derived from CEOF analysis.

Secondly, in 2003, when a severe European HW persisted from June to August with devastating impacts stands out as an anomalous climatic event (Bastos et al., 2003). This HW event is confined to the western part of the Eurasian continent and its propagation feature do not stand out over the Eurasia continent. The severe 2003 European summer HW also found to be affected by the atmospheric stationary wave (Shi et al., 2024). Besides, in 2010, although the HW events occurred in June show eastward propagation characteristics (Fig. 16), the HW event that persisted from July to mid-August over Eurasia is quasi-stationary. The maximum value of the metric in 2010 is likely to be affected by this stationary variability due to the intrinsic limitation of the present method. The amplitude metric effectively captures the year when strong propagating variability occurs but can be influenced by stationary variability. This is an intrinsic limitation from the fact that the standing oscillation of a unit amplitude can also be expressed by the superposition of the two propagating oscillations into opposite directions with half amplitudes. To evaluate the connection between propagating signals of intraseasonal air temperature oscillation and propagating HWs, a quantitative skill metric is needed. Finally, HWs and droughts often occur together, and their combined effects, recently noted as compound drought and HWs, have drawn increasing attention (Miralles et al., 2014; Mukherjee et al., 2020). Such events have also been identified over Eurasia (Schubert et al., 2014). In addition, the CEOF analysis is also employed to understand the evolution of the spatiotemporal characteristics of droughts over East Asia (Zhou et al., 2021). Furthermore, the latent heating rate, which is directly related to the total amount of condensation of water vapor and is closely related to the precipitation, plays a compensatory role in the air temperature eastward propagating oscillation (Figs. 8a and 8e). This suggests that we need to consider the propagating

signals of both air temperature and precipitation over Eurasia. A more thorough analysis could provide deeper insights and improve our understanding of how such extreme events evolve and interact.

Data Availability Statement

Validation datasets including daily maximum temperature data can be obtained from the CPC and are available via the NOAA ESRL climate data repository (https://www.esrl.noaa.gov/psd/data/gridded/data.cpc.globaltemp.html). The other meteorological data retrieved from the JRA-55 are available at https://jra.kishou.go.jp/JRA-55/index_en.html. The ERA5 dataset can be found at https://cds.climate.copernicus.eu/cdsapp#!/dataset/reanalysis-era5-pressure-levels?tab=overview.

Acknowledgments

I want to express my most sincere gratitude to my academic supervisor, Professor Shoshiro Minobe, for his many valuable suggestions and discussions throughout the study. Without his support, I could not complete my Ph.D. study. I would also like to thank my Ph.D. committee, Profs: Masaru Inatsu, Yoshinori Sasaki, and Yousuke Sato. Finally, I wish to express my thanks to my parents.

References

Barnett TP (1983) Interaction of the monsoon and Pacific trade wind system at interannual time scales part I: The equatorial zone. Mon Wea Rev 111(4):756-773. https://doi.org/10.1175/1520-0493(1983)111<0756:IOTMAP>2.0.CO;2.

Barriopedro D, Fischer EM, Luterbacher J, Trigo RM, García-Herrera R (2011) The hot summer of 2010: redrawing the temperature record map of Europe. Science 332(6026):220-224. https://doi.org/10.1126/science.1201224.

Bretherton CS, Widmann M, Dymnikov VP, Wallace JM, Bladé I (1999) The effective number of spatial degrees of freedom of a time-varying field. J Clim 12(7):1990-2009. https://doi.org/10.1175/1520-0442(1999)012<1990:TENOSD>2.0.CO;2.

Ding Q, Wang B (2007) Intraseasonal teleconnection between the summer Eurasian wave train and the Indian monsoon. J Clim 20:3751–3767. https://doi.org/10.1175/JCLI4221.1.

Dole R, Hoerling M, Perlwitz J, Eischeid J, Pegion P, Zhang T, Quan XW, Xu T, Murray D (2011) Was there a basis for anticipating the 2010 Russian heat wave? Geophys Res Lett 38:L06702. https://doi.org/10.1029/2010GL046582.

Dommenget D, Latif M (2002) A cautionary note on the interpretation of EOFs. J Climate 15(2):216-225. https://doi.org/10.1175/1520-0442(2002)015<0216:ACNOTI>2.0.CO;2.

Dong B, Sutton RT, Shaffrey L (2022) Recent decadal weakening of the summer Eurasian westerly jet attributable to anthropogenic aerosol emissions. Nat Commun 13:1148. https://doi.org/10.1038/s41467-022-28816-5

Enfield DB, Mestas-Nuñez AM (1999) Multiscale variabilities in global sea surface temperatures and their relationships with tropospheric climate patterns. J Clim 12:2719–2733, https://doi.org/10.1175/1520-0442(1999)012<2719:MVIGSS>2.0.CO;2.

Fan L, Yang S (2023) Impact of Westward-Propagating ISO over Mid-High-Latitude Eurasia on SSW during Boreal Winter. J Climate 36:6797–6816. https://doi.org/10.1175/JCLI-D-22-0843.1.

Fujinami H, Yasunari T (2004) Submonthly variability of convection and circulation over and around the Tibetan Plateau during the boreal summer. Journal of the Meteorological Society of Japan Ser II 82(6):1545-1564. https://doi.org/10.2151/jmsj.82.1545.

Fukutomi Y, Masuda K, Yasunari T (2012) Spatiotemporal structures of the intraseasonal oscillations of precipitation over northern Eurasia during summer. Int J Climatol 32:710-726. https://doi.org/10.1002/joc.2293.

Hannachi A, Jolliffe IT, Stephenson DB (2007) Empirical orthogonal functions and related techniques in atmospheric science: A review. Int J Climatol 27:1119-1152. https://doi.org/10.1002/joc.1499.

Harada Y, Kamahori H, Kobayashi C, Endo H, Kobayashi S, Ota Y, Onoda H, Onogi K, Miyaoka K, Takahashi K (2016) The JRA-55 Reanalysis: Representation of atmospheric circulation and climate variability. J Meteor Soc Japan Ser II 94(3):269-302. https://doi.org/10.2151/jmsj.2016-015.

Horel JD (1984) Complex principal component analysis: Theory and examples. J Appl Meteor Climatol 23(12):1660-1673.

Hu W, Duan A, Li Y, He B (2016) The intraseasonal oscillation of eastern Tibetan Plateau precipitation in response to the summer Eurasian wave train. J Clim 29:7215–7230.

Huang DQ, Zhu J, Zhang YC, Huang AN (2014) The different configurations of the East Asian polar front jet and subtropical jet and the associated rainfall anomalies over eastern China in summer. J Climate 27:8205-8220. https://doi.org/10.1175/JCLI-D-14-00067.1.

Iwao K, Takahashi M (2008) A Precipitation Seesaw Mode between Northeast Asia and Siberia in Summer Caused by Rossby Waves over the Eurasian Continent. J Climate 21:2401–2419. https://doi.org/10.1175/2007JCLI1949.1.

Jiang X, Lau NC (2008) Intraseasonal teleconnection between North American and western North Pacific monsoons with 20-day time scale. J Climate 21:2664–2679. https://doi.org/10.1175/2007JCLI2024.1.

Kikuchi K, Wang B (2009) Global perspective of the quasi-biweekly oscillation. J Clim 22:1340–1359.

Kirkyla KI, Hameed S (1989) Harmonic analysis of the seasonal cycle in precipitation over the United States: A comparison between observations and a general circulation model. J Clim 2(12):1463-1475. https://doi.org/10.1175/15200442(1989)002<1463:HAOTSC>2.0.CO;2.

Kobayashi S, Ota Y, Harada Y, Ebita A, Moriya M, Onoda H, Onogi K, Kamahori H, Kobayashi C, Endo H, Miyaoka K (2015) The JRA-55 reanalysis: General specifications and basic characteristics. J Meteor Soc Japan Ser II 93(1):5-48. https://doi.org/10.2151/jmsj.2015-001.

Kornhuber K, Osprey S, Coumou D, Petri S, Petoukhov V, Rahmstorf S, Gray L (2019) Extreme weather events in early summer 2018 connected by a recurrent hemispheric wave-7 pattern. Environ Res Lett 14(5):054002. https://doi.org/10.1088/1748-9326/ab13bf.

Li J, Mao J (2019) Coordinated influences of the tropical and extratropical intraseasonal oscillations on the 10-30-day variability of the summer rainfall over southeastern China. Clim Dyn 53:137–153. https://doi.org/10.1007/s00382-018-4574-8.

Liang P, Lin H, Ding Y (2018) Dominant modes of subseasonal variability of East Asian summertime surface air temperature and their predictions. J Clim 31:2729–2743. https://doi.org/10.1175/JCLI-D-17-0368.1.

Liu B, Yan Y, Zhu C, Ma S, Li J (2020) Record‐breaking Meiyu rainfall around the Yangtze River in 2020 regulated by the subseasonal phase transition of the North Atlantic Oscillation. Geophys Res Lett 47.

O'Kane TJ, Matear RJ, Chamberlain MA, Oliver ECJ, Holbrook N (2014) Storm tracks in the Southern Hemisphere subtropical oceans. University of Tasmania. Journal contribution. https://hdl.handle.net/102.100.100/574826.

Majumder S, Goes M, Polito PS, Lumpkin R, Schmid C, Lopez H (2019) Propagating modes of variability and their impact on the western boundary current in the South Atlantic. J Geophys Res: Oceans 124(5):3168-3185. https://doi.org/10.1029/2018JC014812.

Minobe S, Ogawa F, Enomoto T, Miyama T, Nakano M, Sekizawa S, Yamazaki A (2022) Unprecedented Heatwave Around Northern Japan in Summer 2021 and its Global Linkages. Preprint at https://papers.ssrn.com/sol3/papers.cfm?abstract_id=4100359.

Namias J (1950) The index cycle and its role in the general circulation. J Meteor Sci 7:130–139. https://doi.org/10.1175/1520-0469(1950)007<0130:TICAIR>2.0.CO;2.

Navarra A, Simoncini V (2010) A guide to empirical orthogonal functions for climate data analysis. Springer Science & Business Media.

North GR, Bell TL, Cahalan RF, Moeng FJ (1982) Sampling errors in the estimation of empirical orthogonal functions. Mon Wea Rev 110:699-706. https://doi.org/10.1175/1520-0493(1982)110<0699:SEITEO>2.0.CO;2.

Orsolini Yvan J, Sorteberg Asgeir (2009) Projected Changes in Eurasian and Arctic Summer Cyclones under Global Warming in the Bergen Climate Model, Atmospheric and Oceanic Science Lett 2(1):62-67. https://doi.org/10.1080/16742834.2009.11446776.

Qi X, Yang J (2019) Extended-range prediction of a heat wave event over the Yangtze River Valley: Role of intraseasonal signals. Atmos Oceanic Sci Lett 12:451–457. https://doi.org/10.1080/16742834.2019.1669408.

Rasmusson EM, Arkin PA, Chen WY, Jalickee JB (1981) Biennial variations in surface temperature over the United States as revealed by singular decomposition. Mon Wea Rev 109(3):587-598. https://doi.org/10.1175/1520-0493(1981)109<0587:BVISTO>2.0.CO;2.

Rex DF (1950) Blocking action in the middle troposphere and its effects on regional climate, I: An aerological study of blocking. Tellus 2:196-211.

Stefanon M, Fabio D, Drobinski P (2012) Heatwave classification over Europe and the Mediterranean region. Environ Res Lett 7(1):014023. https://doi.org/10.1088/1748-9326/7/1/014023.

Susanto RD, Zheng Q, Yan XH (1998) Complex singular value decomposition analysis of equatorial waves in the Pacific observed by TOPEX/Poseidon altimeter. J Atmos Oceanic Technol 15(3):764-774. https://doi.org/10.1175/1520-0426(1998)015<0764:CSVDAO>2.0.CO;2.

Teng H, Branstator G, Wang H, Meehl GA, Washington WM (2013) Probability of US heat waves affected by a subseasonal planetary wave pattern. Nat Geosci 6:1056–1061. https://doi.org/10.1038/ngeo1988.

Terradas J, Oliver R, Ballester JL (2004) Application of statistical techniques to the analysis of solar coronal oscillations. The Astrophysical Journal 614(1):435. https://doi.org/10.1086/423332.

Vitart F, Robertson AW (2018) The sub-seasonal to seasonal prediction project (S2S) and the prediction of extreme events. npj Clim Atmos Sci 1:3. https://doi.org/10.1038/s41612-018-0013-0.

Wang P, Tang J, Sun X, Wang S, Wu J, Dong X, Fang J (2017) Heat waves in China: Definitions, leading patterns and connections to large-scale atmospheric circulation and SSTs. J Geophys Res: Atmos 122(10):679–10,699. https://doi.org/10.1002/2017JD027180.

Wang X, Zhang R, Jin D, Zhang Y (2023) An Intraseasonal Dipole Mode in Summertime Surface Air Temperature over Eurasia and Its Association with Heat Wave Occurrence. J Clim 36:7755–7770. https://doi.org/10.1175/JCLI-D-22-0761.1.

Watanabe M (2004) Asian Jet Waveguide and a Downstream Extension of the North Atlantic Oscillation. J Climate 17:4674–4691. https://doi.org/10.1175/JCLI-3228.1.

White RH, Kornhuber K, Martius O, Wirth V (2022) From atmospheric waves to heatwaves: A waveguide perspective for understanding and predicting concurrent, persistent, and extreme extratropical weather. Bull Amer Meteor Soc 103(3):E923-E935. https://doi.org/10.1175/BAMS-D-21-0170.1.

Xiu J, Jiang X, Zhang R, Guan W, Chen G (2022) An intraseasonal mode linking wintertime surface air temperature over Arctic and Eurasian continent. J Clim 35:2675–2696. https://doi.org/10.1175/JCLI-D-21-0495.1.

Xu P, Wang L, Chen W, Chen G, Kang L (2020) Intraseasonal Variations of the British–Baikal Corridor Pattern. J Climate 33:2183–2200. https://doi.org/10.1175/JCLI-D-19-0458.1.

Yang S, Wen X, Gao M (2022) Relation of Mid-High-Latitude Eurasian ISO to Ural Blocking Frequency and Their Co-Effect on Extreme Hot Events during Boreal Summer. Atmosphere 13:2041. https://doi.org/10.3390/ atmos13122041.

Yao S, Sun Q, Huang Q, Chu P (2016) The 10-30-day intraseasonal variation of the East Asian winter monsoon: The temperature mode. Dyn. Atmos Oceans 75:91-101. https://doi.org/10.1016/j.dynatmoce.2016.07.001.

Yang SY, Wu BY, Zhang RH (2013) The zonal propagating characteristics of low-frequency oscillation over the Eurasian mid-high latitude in boreal summer. Science China: Earth Sciences. https://doi.org/10.1007/s11430-012-4576-z.

Zhao C, Li T, Yao S, Behera SK, Nasuno T (2017) Intraseasonal variability of air temperature over East Asia in boreal summer. Front. Earth Sci 5:63–74.

Zhu T, Yang J, (2021) Two types of mid-high-latitude low-frequency intraseasonal oscillations near the Ural Mountains during boreal summer. J Clim 34:4279-4296. https://doi.org/10.1175/JCLI-D-20-0589.1.

Zhu T, Yang J, Wang B, Bao Q (2023) Boreal summer extratropical intraseasonal waves over the Eurasian continent and real-time monitoring metrics. J Clim 36(12):3971-3991. https://doi.org/10.1175/JCLI-D-22-0788.1.

Figures

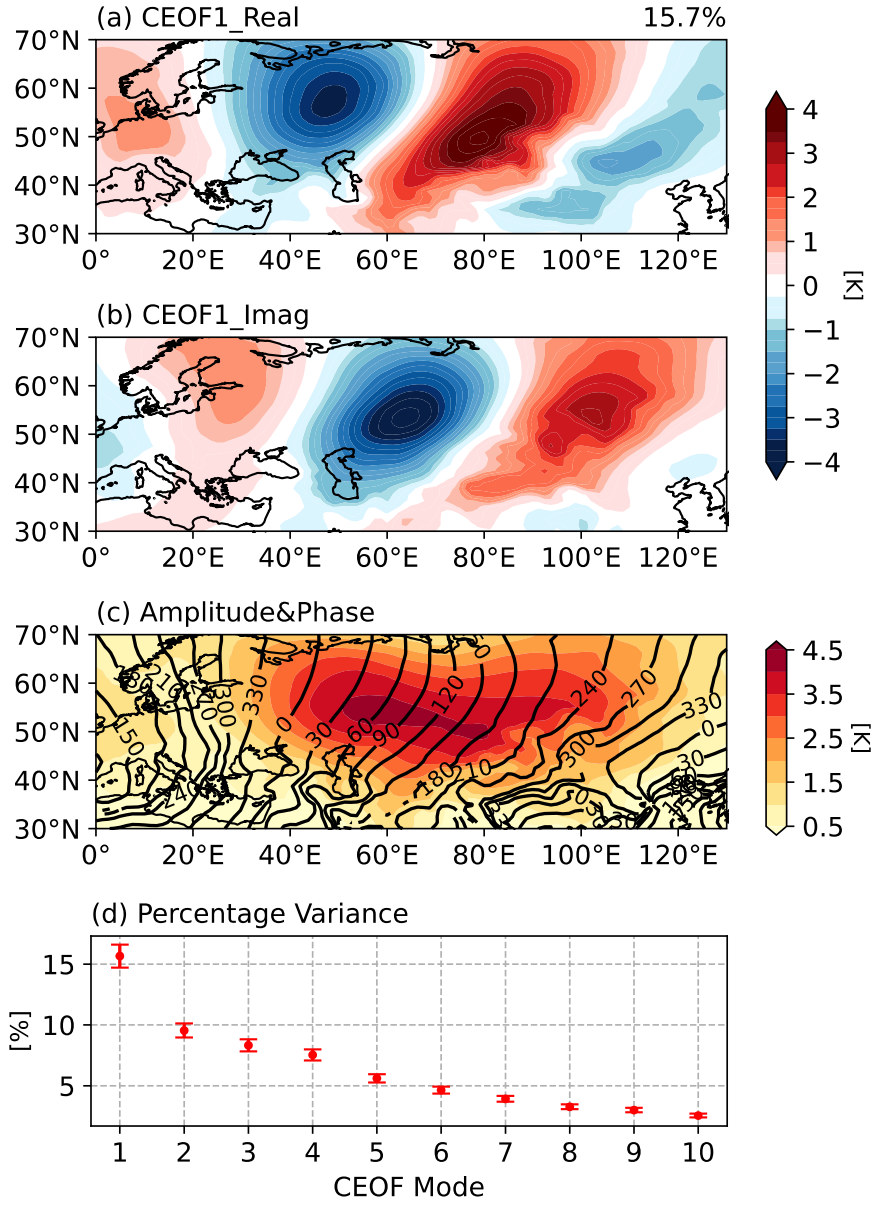


Figure 1 | The spatial patterns of (a) the real part, (b) imaginary part, and (c) the spatial amplitude (shading; unit: K) and phase (contours) of the CEOF-1 of the 850 hPa air mean temperature anomalies for JJA from 1979 to 2021 using JRA-55 dataset. (d) Percentage variance (unit: %) explained by the first 10 CEOF modes and the associated error ranges (bars).

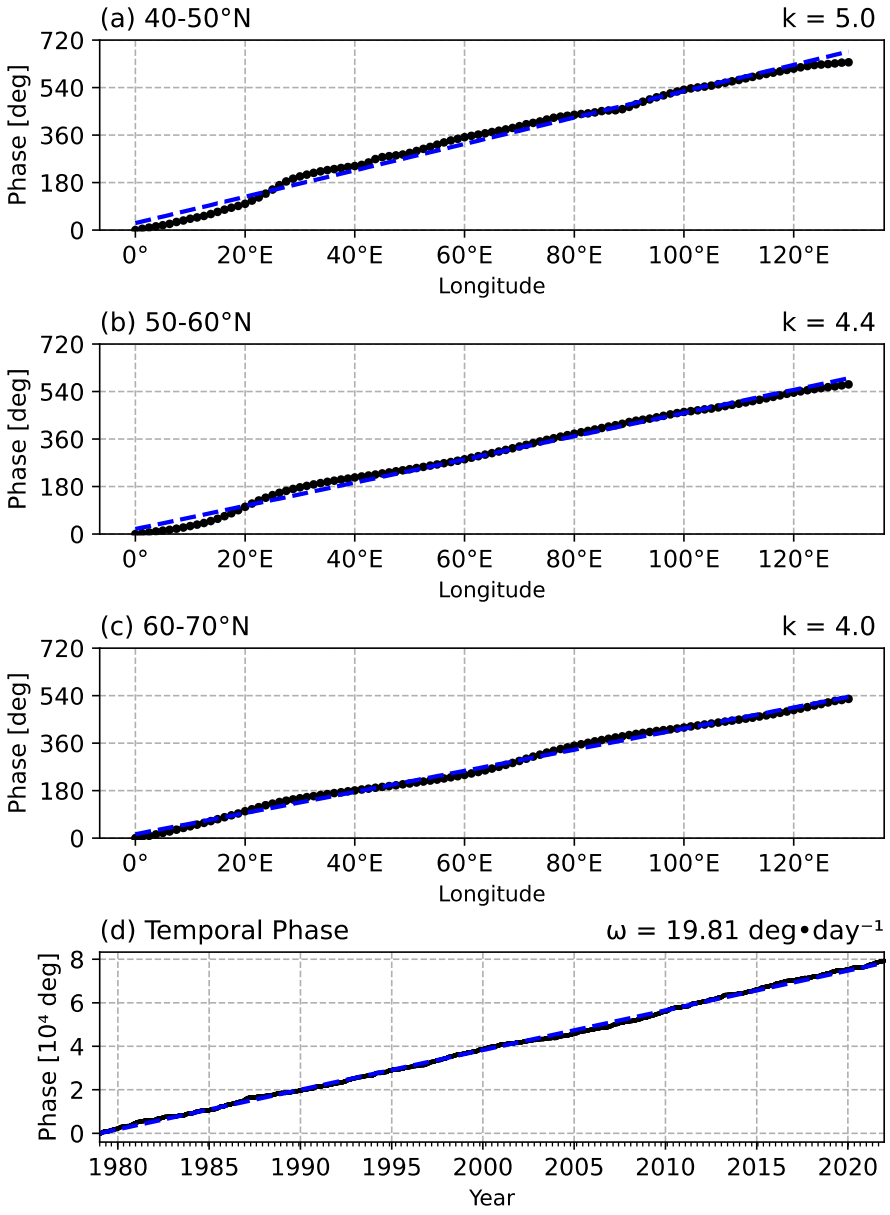


Figure 2 | (a-c) The spatial phases of the CEOF-1 (black dotted lines) with latitudinal averaged at 40-50°N, 50-60°N, and 60-70°N. (d) The temporal phases of the CPC-1. The unit of the wavenumber k in (a-c) is deg (° longitude)$^{-1}$. The blue dashed lines are their linear fits calculated by linear regressions.

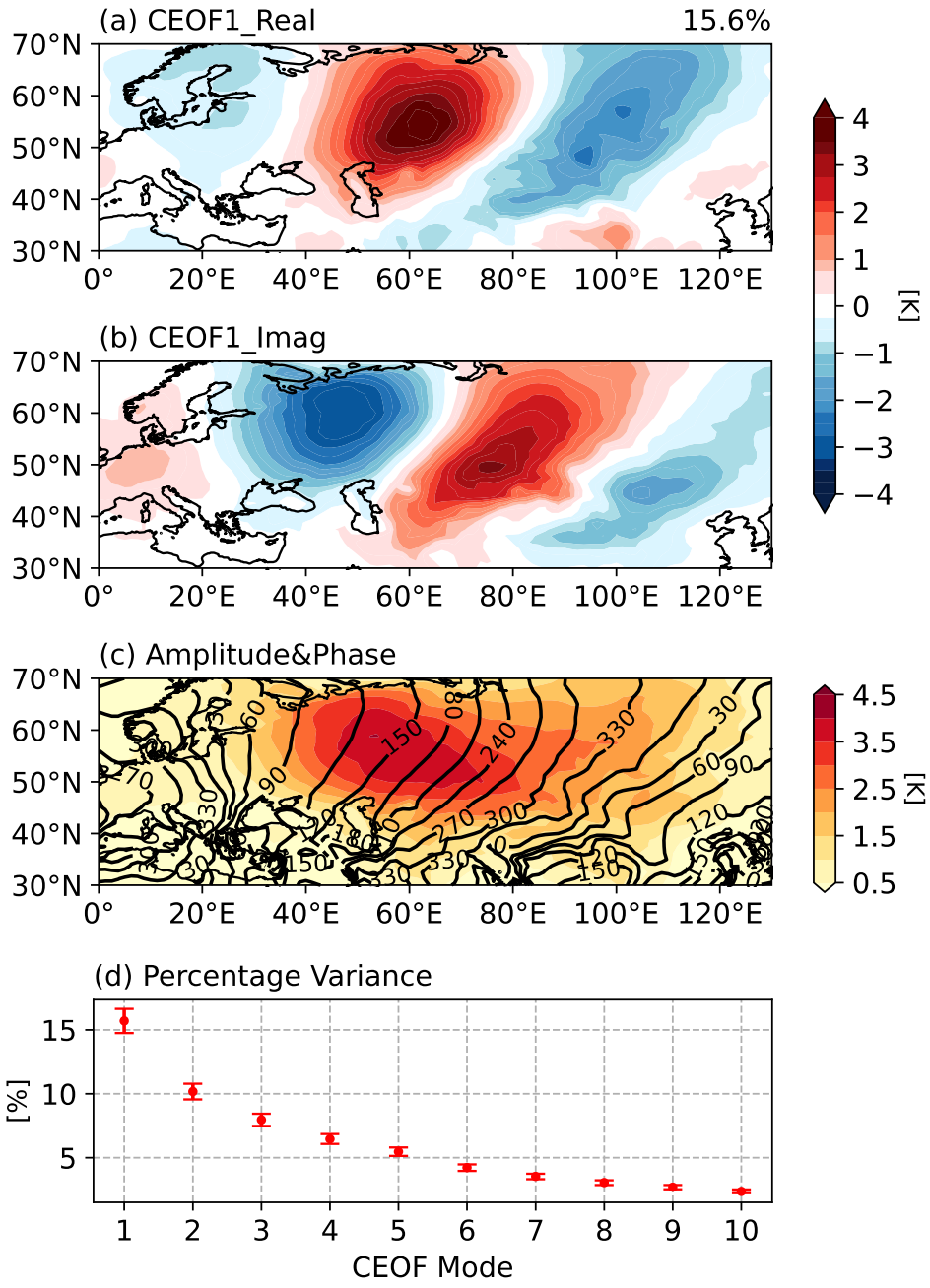


Figure 3 | Similar to Fig. 1 but for 2-m air mean temperature.

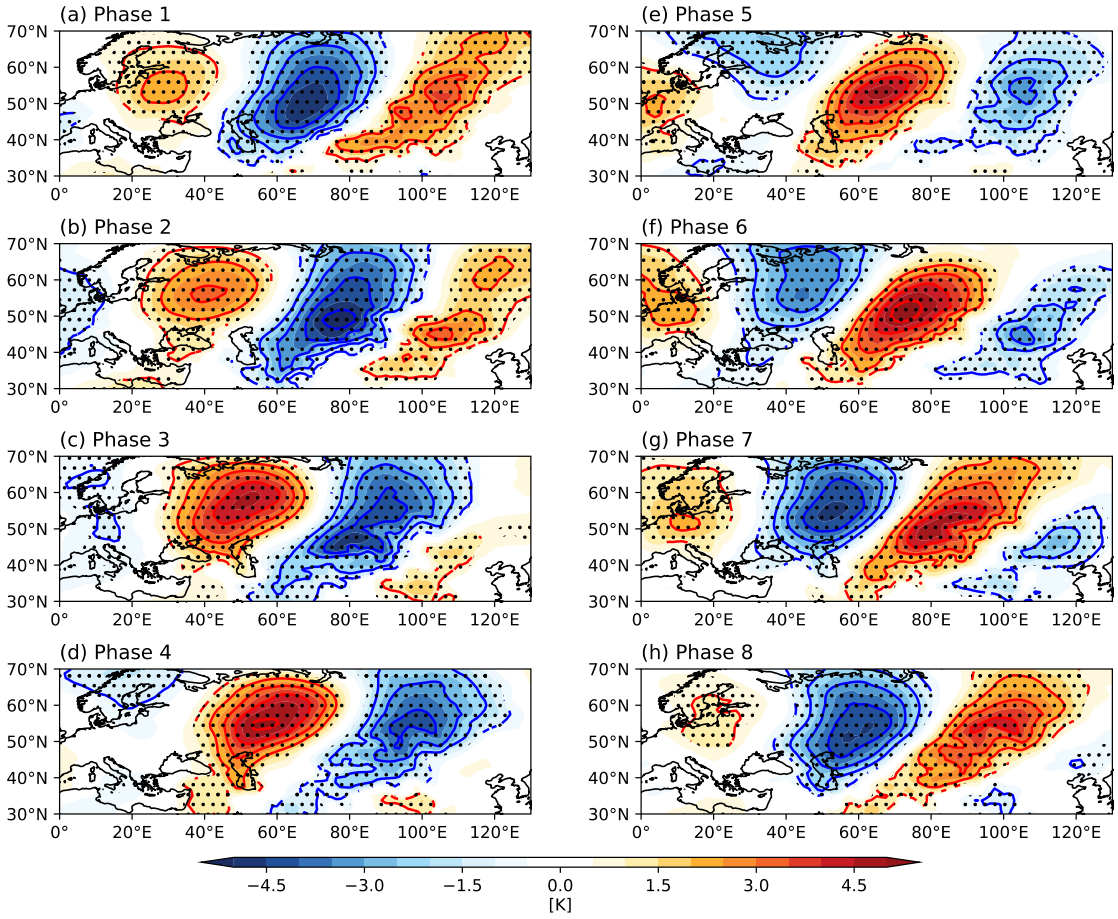


Figure 4 | Composite analysis of air temperature at 850 hPa (shading; unit: K) and geopotential heights at 200 hPa (contours, unit: gpm) from phase 1 to 8. The red (blue) contours are the positive (negative) values. Only the 200 hPa geopotential height anomaly above the 99% confidence level is given. The dots indicate the regions where air temperature anomaly are significance at the 99% confidence level.

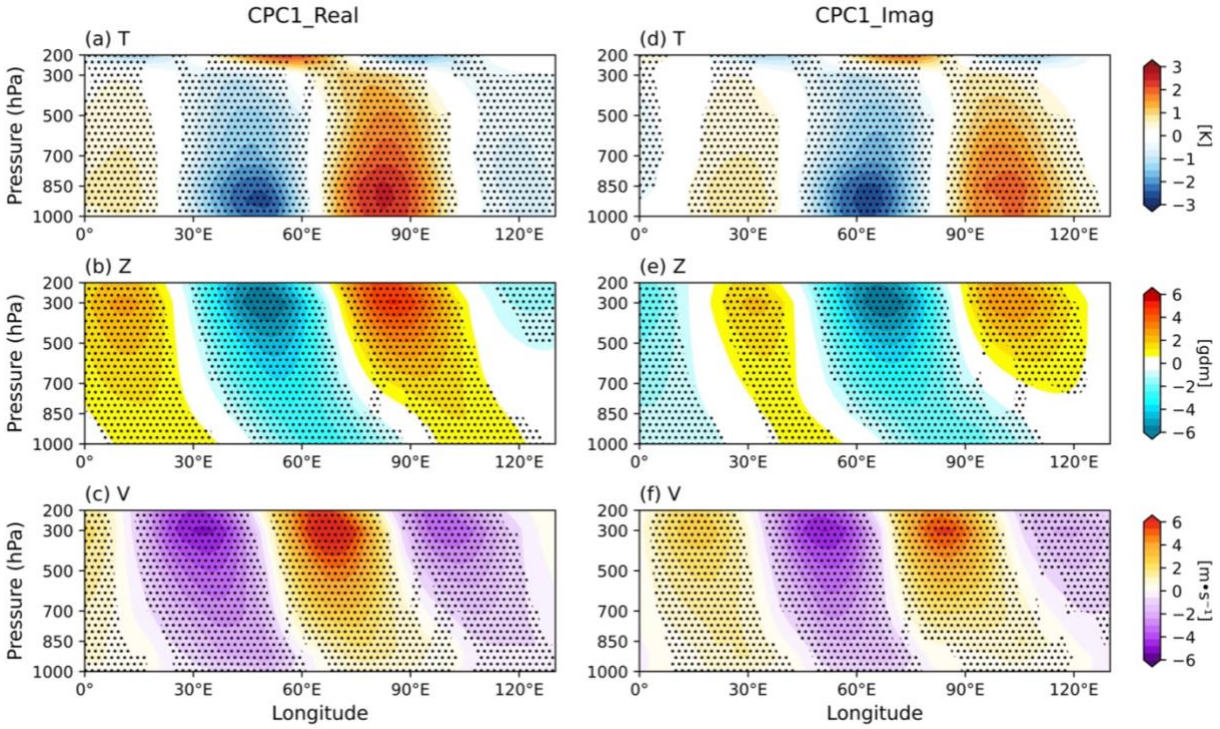


Figure 5 | Regression maps of the 850 hPa (a) air temperature (unit: K), (b) geopotential height (unit: gdm), and (c) meridional wind (unit: m s^{-1}) anomalies on the normalized real and imaginary components of CPC-1 of 850 hPa air temperature anomalies during JJA from 1979 to 2021. The dots indicate significance at the 99% confidence level.

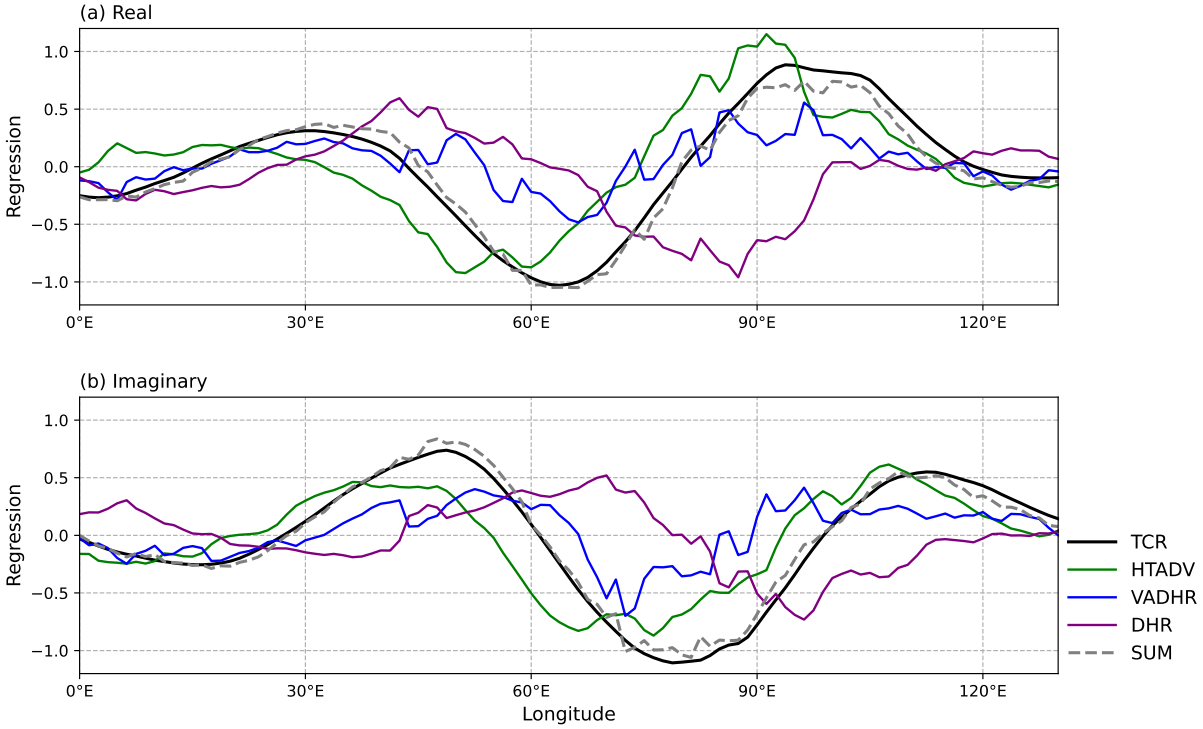


Figure 6 | The latitudinal averaged values for air temperature changing rate (TCR; black line), horizontal temperature advection (HTADV; green line), vertical component in adiabatic heating rate (VADHR; blue line), and diabatic heating rate anomalies (DHR; purple line) at 850 hPa (units: K day^{-1}) between 40-70°N for CPC-1 (a) Real and (b) Imaginary amplitudes. The gray dashed line is the sum of values of horizontal temperature advection, vertical component in adiabatic heating rate , and diabatic heating rate anomalies.

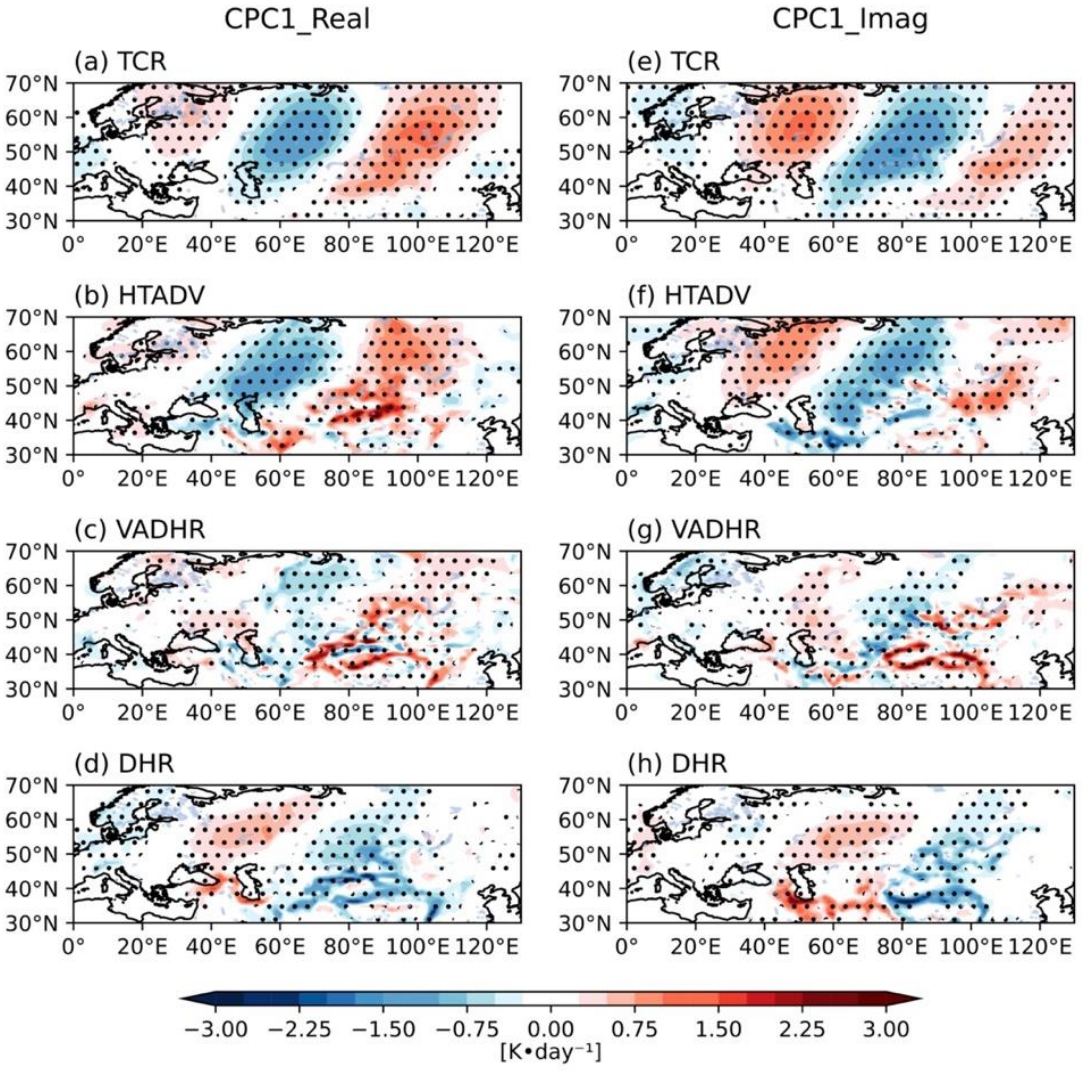


Figure 7 | Regression maps of the (a) air temperature changing rate (TCR), (b) horizontal temperature advection (HTADV), (c) vertical component in adiabatic heating rate (VADHR), and (d) diabatic heating rate anomalies (DHR) at 850 hPa (units: K day^{-1}) on the normalized real (left) and imaginary (right) CPC-1 of 850 hPa air temperature anomalies during JJA from 1979 to 2021. The dots indicate significance at the 99% confidence level.

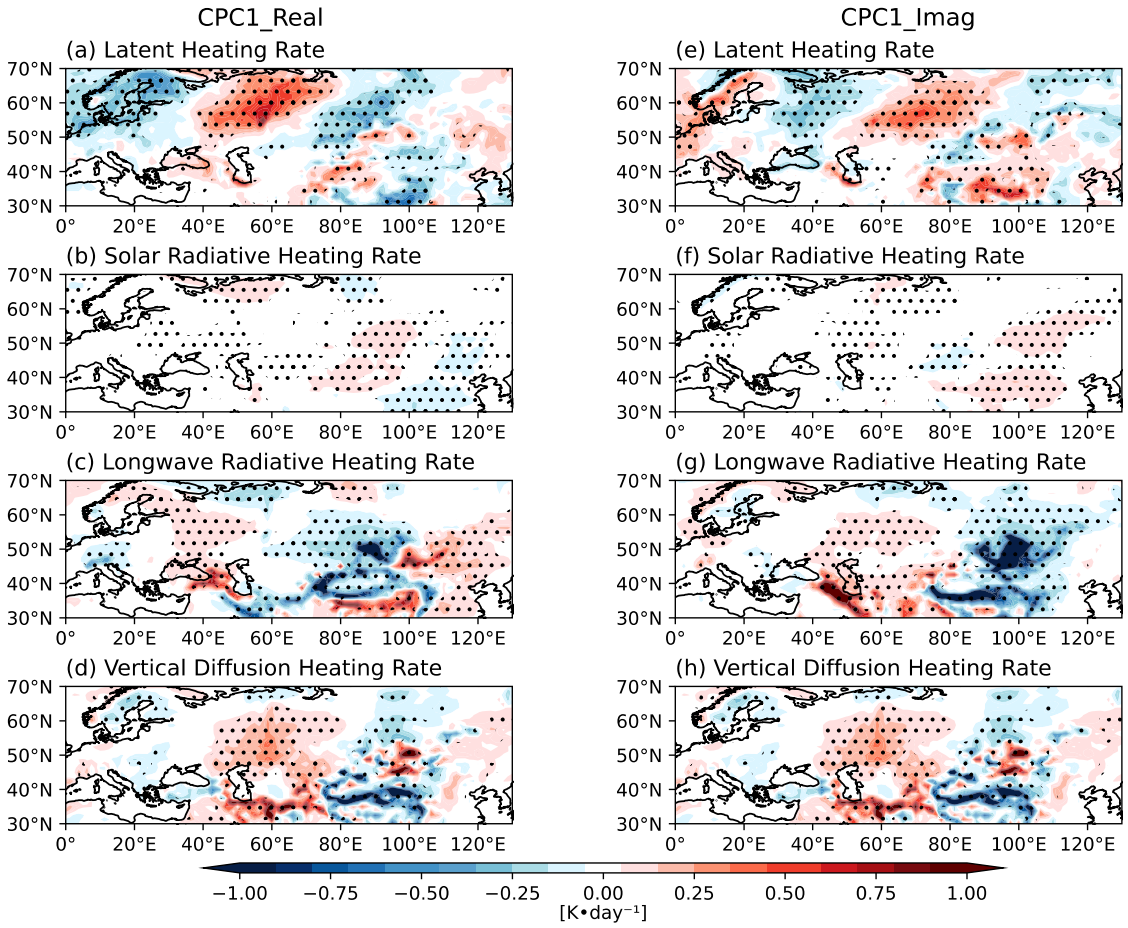


Figure 8 | Similar to Fig. 7 but for (a) latent heating rate, (b) solar radiative heating rate, (c) longwave radiative heating rate, and (d) vertical diffusion heating rate anomalies at 850 hPa (units: K day^{-1}).

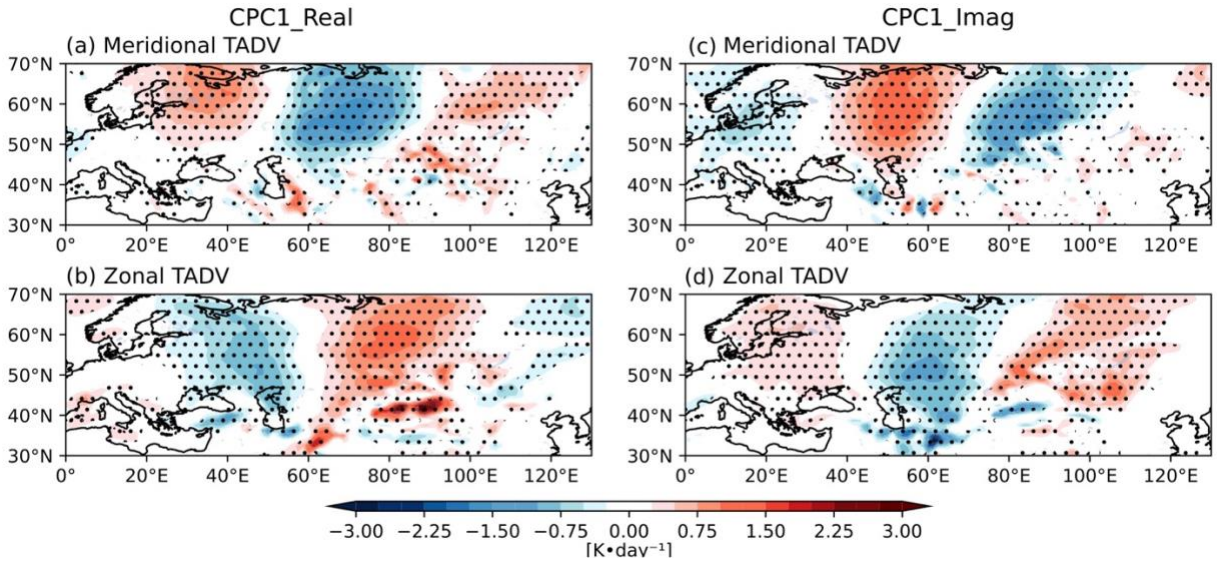


Figure 9 | Similar to Fig. 7 but for (a) meridional temperature advection and (b) zonal temperature advection anomalies at 850 hPa (units: K day^{-1}).

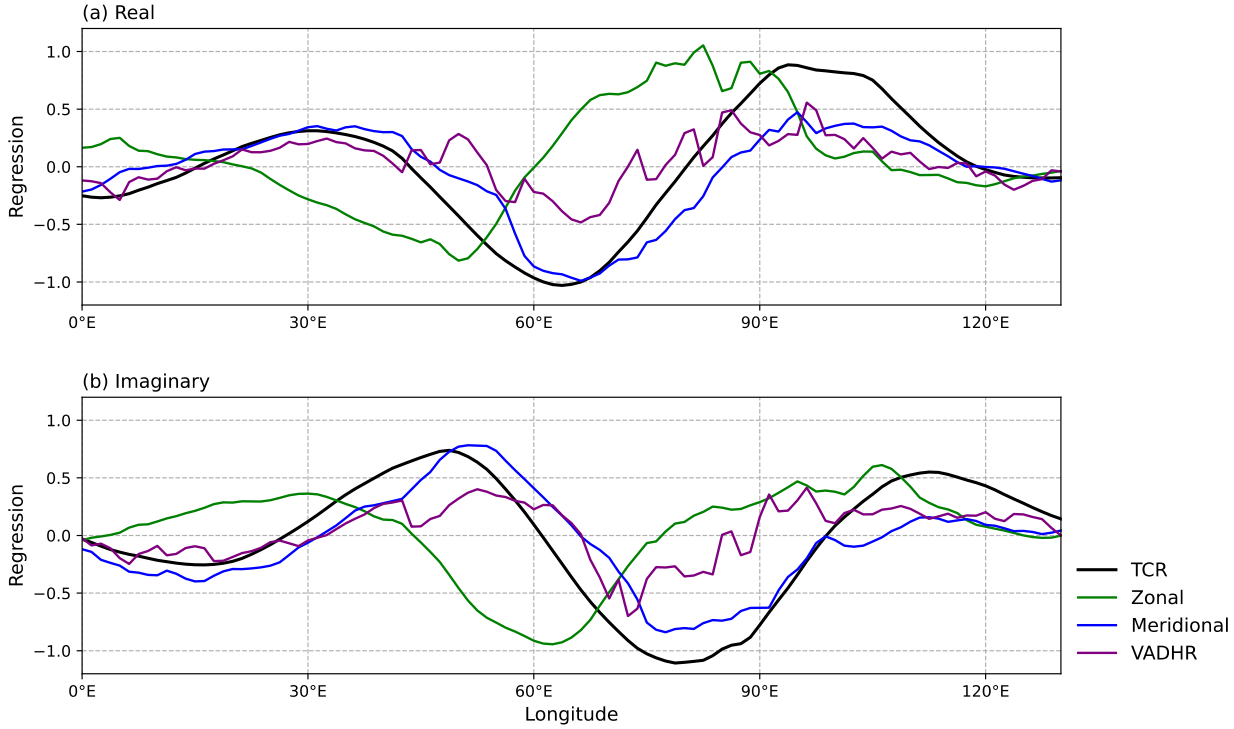


Figure 10 | Similar to Fig. 6 but for temperature changing rate (black line), meridional temperature advection (blue line), zonal temperature advection (green line), vertical component in adiabatic heating rate (purple line) anomalies at 850 hPa (units: K day^{-1}).

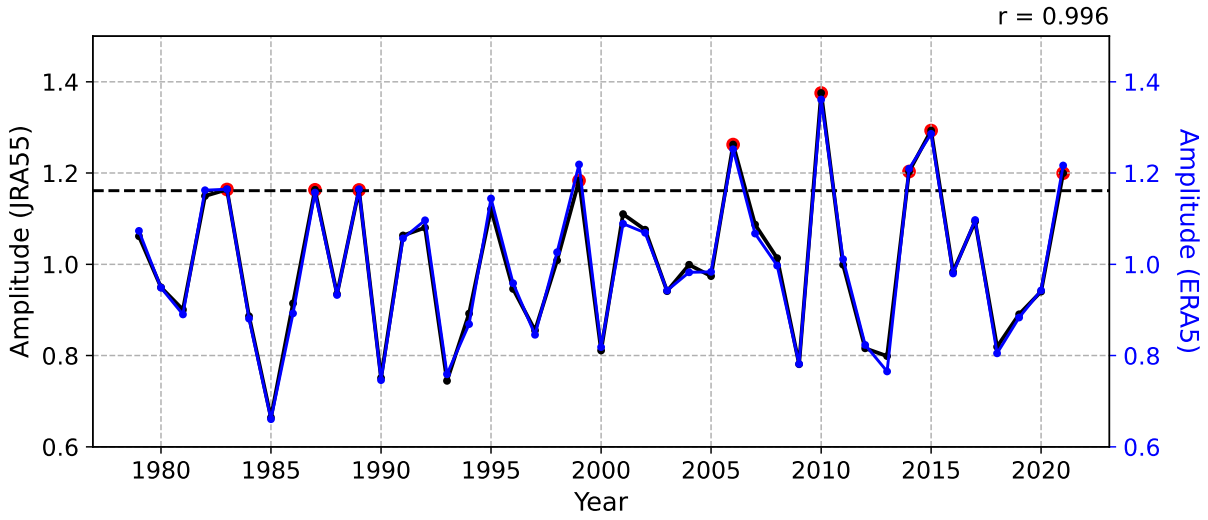


Figure 11 | The absolute amplitude of CPC-1 averaged for each summer (black line for JRA55 and blue line for ERA5). Red dots indicate values exceeding one standard deviation above the average of the amplitude metric derived from JRA-55.

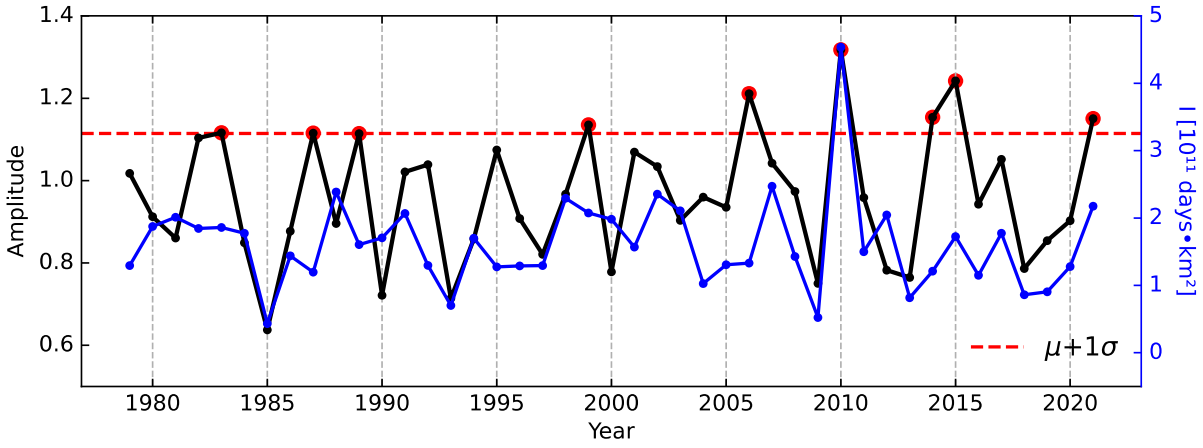


Figure 12 | The absolute amplitude of CPC-1 averaged for each summer (black line). Time series of area-weighted time-area integrated accumulated HW days (blue line; unit: day km^2) over 40-70°N, 0-130°E computed by taking an area sum after weighting each grid-cell area by the cosine of its latitude. Red dashed line indicates that one standard deviation above the average of the amplitude metric, and red dots indicate values exceeding this threshold.

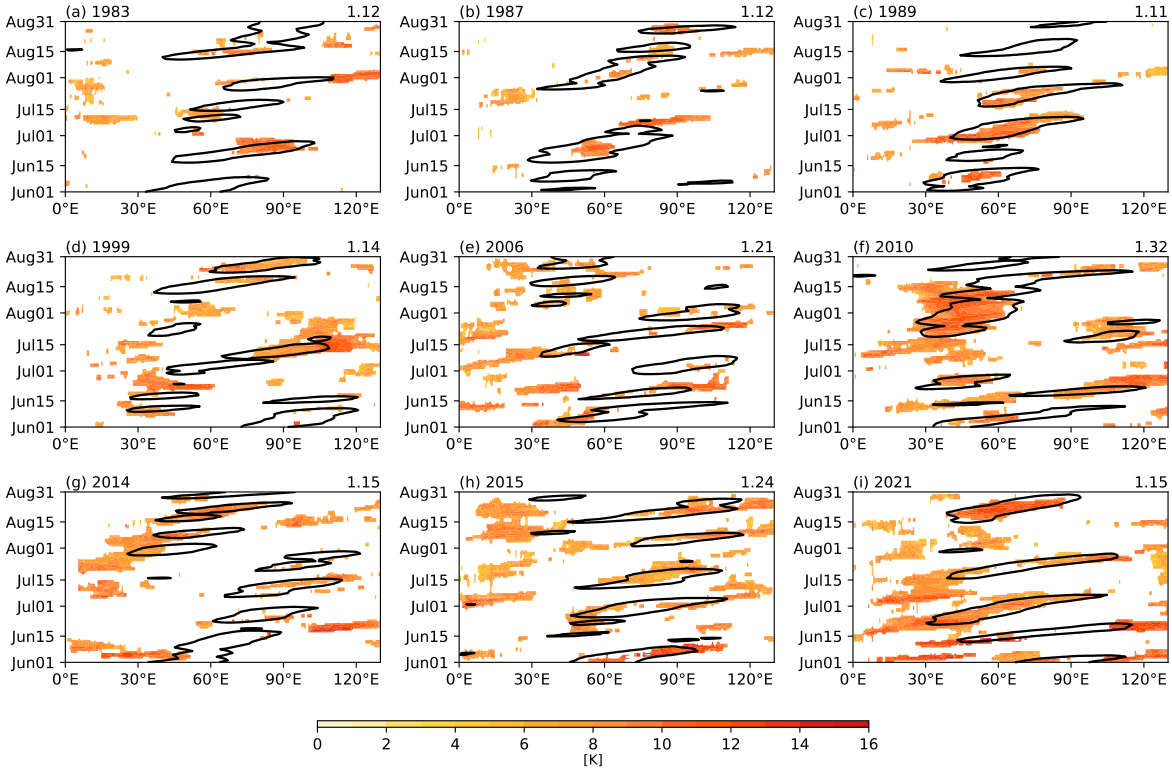


Figure 13 | Time-longitude section of the daily 2-m maximum temperature anomalies (unit: K) that satisfy the HW condition and reconstructed 850 hPa air temperature anomalies of CEOF-1 (contours with value 2 K) averaged from 40-70°N for years (a) 1983, (b) 1987, (c) 1989, (d) 1999, (e) 2006, (f) 2010, (g) 2014, (h) 2015, and (i) 2021. The values displayed here are the values of the amplitude metric in Fig. 11.

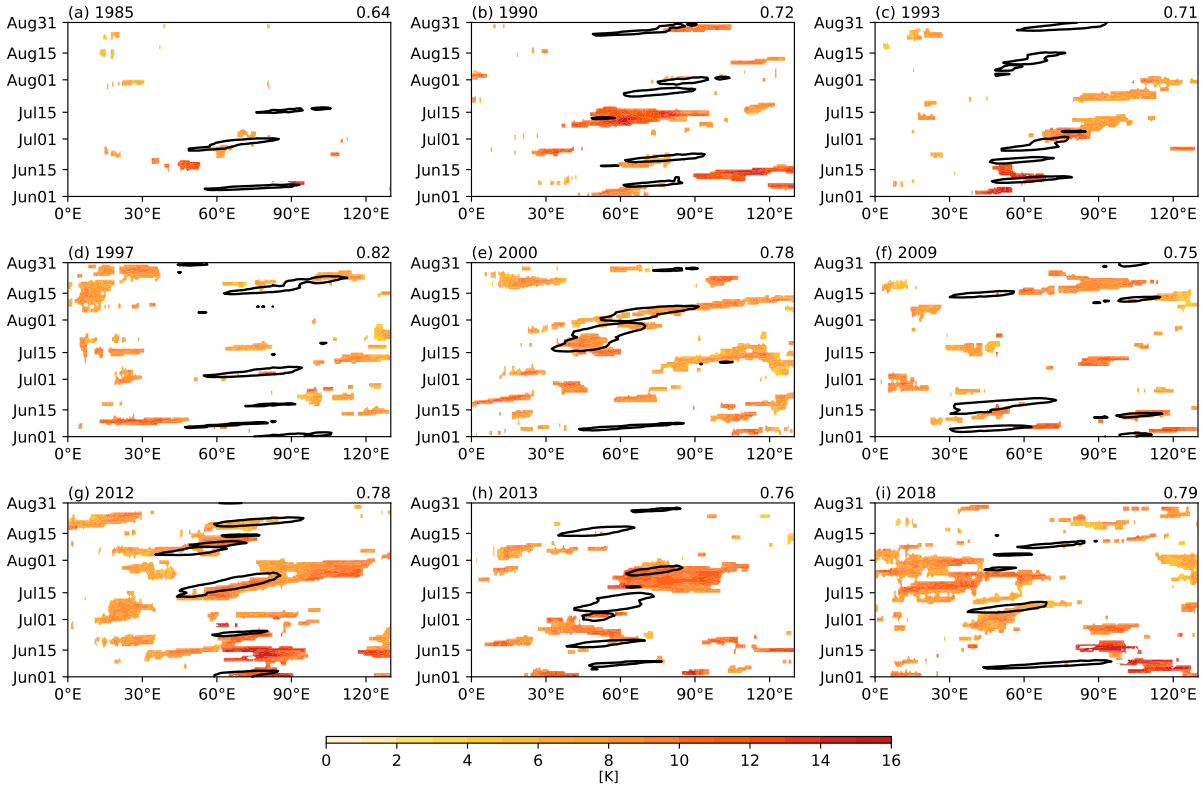


Figure 14 | Similar to Fig. 13 but for years (a) 1985, (b) 1990, (c) 1993, (d) 1997, (e) 2000, (f) 2009, (g) 2012, (h) 2013, and (i) 2018.

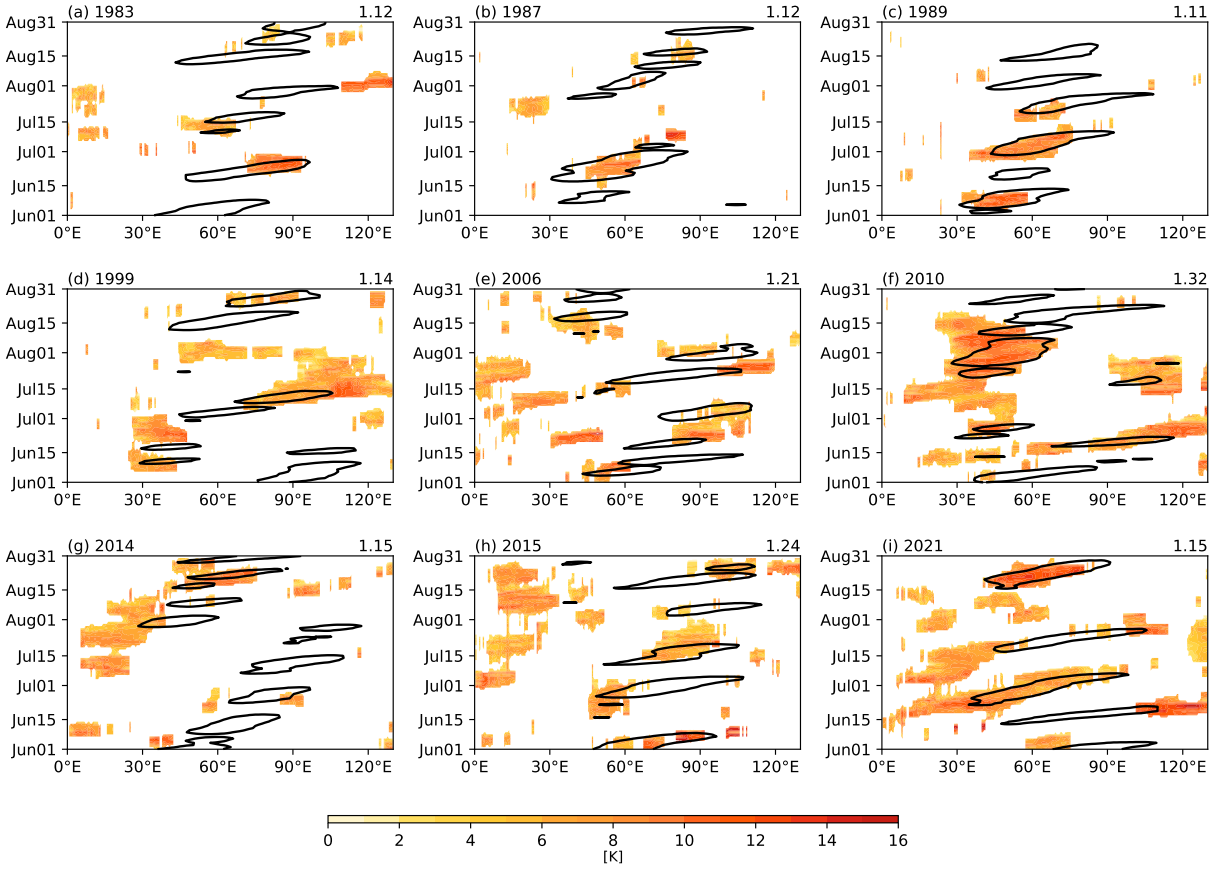


Figure 15 | Similar to Fig. 13 but for different HW condition defined as at least six consecutive days with 2-m mean air temperature exceeding the 90th percentile threshold.

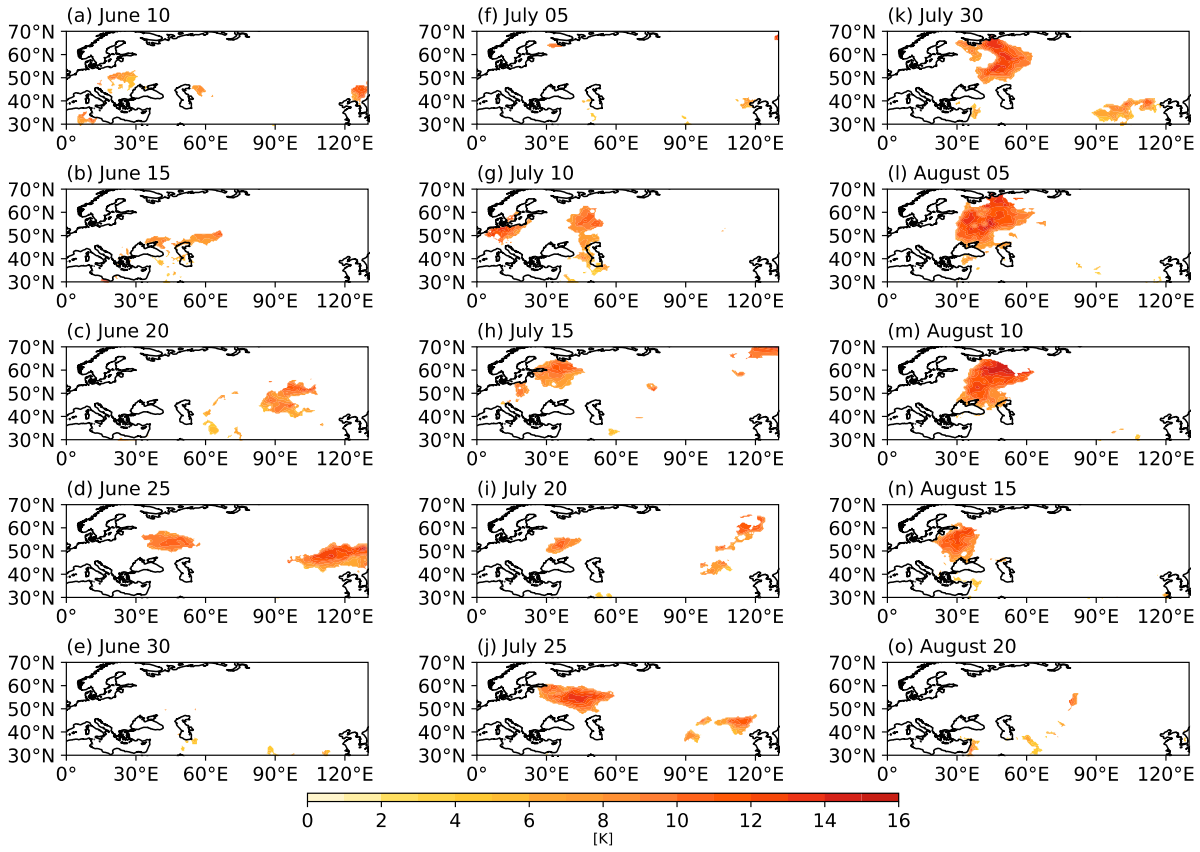


Figure 16 | The spatial patterns of surface air temperature anomalies (units: K) that satisfy HW condition in 2010 from 10th June to 20th August.